Real-space Berry curvature of itinerant electron systems with spin-orbit interaction

Shang-Shun Zhang [1], Hiroaki Ishizuka,[2] Hao Zhang,[1,3] Gábor B. Halász,[3] and Cristian D. Batista[1,4]

[1]*Department of Physics and Astronomy, University of Tennessee, Knoxville, Tennessee 37996-1200, USA*
[2]*Department of Applied Physics, The University of Tokyo, Hongo, Bunkyo, Tokyo, 113-8656, Japan*
[3]*Materials Science and Technology Division, Oak Ridge National Laboratory, Oak Ridge, Tennessee 37831, USA*
[4]*Quantum Condensed Matter Division and Shull-Wollan Center, Oak Ridge National Laboratory, Oak Ridge, Tennessee 37831, USA*

By considering an extended double-exchange model with spin-orbit coupling (SOC), we derive a general form of the Berry phase γ that electrons pick up when moving around a closed loop. This form generalizes the well-known result valid for SU(2) invariant systems, $\gamma = \Omega/2$, where Ω is the solid angle subtended by the local magnetic moments enclosed by the loop. The general form of γ demonstrates that collinear and coplanar magnetic textures can also induce a Berry phase different from 0 or π, smoothly connecting the result for SU(2) invariant systems with the well-known result of Karplus and Luttinger for collinear ferromagnets with finite SOC. By taking the continuum limit of the theory, we also derive the corresponding generalized form of the real-space Berry curvature. The new expression is a generalization of the scalar spin chirality, which is presented in an explicitly covariant form. We finally show how these simple concepts can be used to understand the origin of the spontaneous topological Hall effect that has been recently reported in collinear and coplanar antiferromagnetic phases of correlated materials.

I. INTRODUCTION

The phenomenon of colossal magnetoresistance (CMR) provides a clear example of the dramatic effects of magnetism on electronic transport [1,2]. The ability of changing the longitudinal electric resistivity by several orders of magnitude with an external magnetic field generated a wide interest [3,4], not only due to its multiple technological applications, including magnetic recording, but also because of the rich fundamental physics arising from the interplay between charge and spin degrees of freedom. Indeed, colossal magnetoresistance is an example of the profound influence of quantum mechanics on the macroscopic behavior of correlated materials.

The phenomenon of CMR only refers to the diagonal components of the conductivity tensor. It is natural to ask if a similar dramatic change of the *off-diagonal components of the conductivity tensor* can also be achieved by exploiting the interplay between localized magnetic moments and conduction electrons [5]. Like in the case of CMR materials, the first affirmative answer to this question arose from the study of ferromagnets, whose transverse resistivity contains a term that remains nonzero even after switching off the applied magnetic field [6–8]. Given that the magnetization $\boldsymbol{M}$ is apparently the only axial vector that characterizes the system in absence of the external field, it is not surprising that the observed "anomalous Hall effect" (AHE) turned out to be proportional to $\boldsymbol{M}$. However, subsequent experiments showed that ρ_{xy} can be a nonmonotonic function of M. This key observation led to the discovery of a much more interesting phenomenon of quantum mechanical origin [9].

Karplus and Luttinger made a seminal contribution to the problem of anomalous Hall effect by considering the band structure of ferromagnets in the presence of spin-orbit interaction [10]. They pointed out that the anomalous velocity arises from interband matrix elements of the current operator. Smit provided an alternative explanation of the phenomenon by attributing the AHE to skew scattering with impurities [11]. Later, another extrinsic mechanism, side jump, was proposed by Berger, which is related to the shift of the electron during its collision with an impurity [12]. The skew scattering mechanism leads to a contribution to ρ_{xy} that is proportional to the longitudinal resistivity ρ. In contrast, the intrinsic and side-jump mechanisms give $\rho_{xy} \propto \rho^2$. This behavior of ρ_{xy} was confirmed by a transport measurement in the spinel $CuCe_2Se_{4-x}Br_x$ [13]. In general, the dominant mechanism depends on the material consideration. Our current understanding indicates that skew scattering is dominant in relatively clean materials, while the intrinsic mechanism is dominant in relatively dirty materials [14,15].

The vast implications of the explanation of the AHE offered by Karplus and Luttinger became clear after the derivation of the Hall conductance by Thouless *et al.* and their analysis of the quantum Hall effect [16]. In particular, it was understood that the AHE can be attributed to a Berry phase [17] associated with the Bloch wave functions in solids [18,19]. This Berry phase can arise through different mechanisms. Ye *et al.* [20] proposed a mechanism based on the observation that a carrier moving in a *noncoplanar* spin background acquires a real-space Berry phase, which affects the motion of electrons in the same way as the Aharonov-Bohm [21] phase arising from a physical magnetic field. References [22,23] also discussed the relevance of noncoplanar spin configurations to the AHE in the context of perovskite-type manganites at high temperatures. A similar mechanism was proposed for pyrochlore ferromagnets [9,24] and for noncoplanar

antiferromagnets [25–31]. However, Jungwirth *et al.* [19] showed that noncoplanar spin ordering is not actually necessary to produce an AHE. They related the AHE of *collinear ferromagnets* directly to a Berry phase in momentum space, which arises from the way in which the spin-orbit coupled Bloch wave functions depend on the wave vector. In simple terms, the net spin magnetization of a ferromagnetic system induces an orbital current (or orbital magnetic moment) via the spin-orbit interaction. The combination of a net spin magnetization and SOC then leads to an effective magnetic field which couples to the orbital degrees of freedom of the (spin-polarized) conduction electrons.

In the case of collinear and coplanar magnetic orderings, the SOC can only arise from the *relativistic spin-orbit interaction* [32]. In contrast, the beauty of noncoplanar magnetic orderings is that they produce an effective SOC in absence of any relativistic contribution. This phenomenon arises from the Berry phase γ acquired by the electronic wave function when the electron moves in a closed loop, which cannot be distinguished from the Aharonov-Bohm phase [21] produced by a magnetic flux equal to $\gamma \Phi_0/2\pi$ (Φ_0 is the flux quantum). Given that spins of an elementary plaquette can subtend a solid angle comparable to 2π, the effective magnetic flux produced by a noncoplanar spin ordering can be of the order of one flux quantum per elementary plaquette. For real materials, the area of an elementary plaquette can be as small as a few Å^2, implying that the effective magnetic field produced by a noncoplanar spin ordering can reach values of order 10^5 T. This is an enormous magnetic field if we consider that the strongest pulsed field that can be currently generated in the high magnetic field facilities are slightly higher than 100 T.

The effective gauge field induced by noncoplanar spin orderings [33–35] can be illustrated with the so-called *s-d* exchange model. This idea originates from the seminal papers by Zener [36], and by Anderson and Hasegawa [37], which discuss the double-exchange interaction generated in the limit of large exchange coupling between the local moments and the conduction electrons. In this limit, the spin of the electron is forced to be aligned with the underlying spin field. As a consequence, the effective hopping matrix element between two sites j and k with local classical magnetic moments $\boldsymbol{S}_j = S\boldsymbol{n}_j$ and $\boldsymbol{S}_k = S\boldsymbol{n}_k$ becomes

$$\tilde{t}_{kj} = t_{kj}\langle \boldsymbol{n}_j | \boldsymbol{n}_k \rangle = t_{kj}\cos\left(\chi_{kj}/2\right)e^{i\Omega_{njk}/2}, \qquad (1)$$

where $|\boldsymbol{n}_k\rangle$ is the coherent spin state polarized along the $\boldsymbol{n}_k$ direction $\boldsymbol{S}_k \cdot \boldsymbol{n}_k |\boldsymbol{n}_k\rangle = S|\boldsymbol{n}_k\rangle$, χ_{kj} is the angle between the j and k local moments $\chi_{kj} = \arccos(\boldsymbol{n}_j \cdot \boldsymbol{n}_k)$, and Ω_{njk} is the solid angle subtended by $\boldsymbol{n}_j$, $\boldsymbol{n}_k$, and a reference unit vector $\boldsymbol{n}$. When the electron moves in a closed loop, such as a triangular plaquette, it picks up a Berry phase equal to the sum of the phases Ω_{njk} of each hopping amplitude. This sum is independent of the reference vector $\boldsymbol{n}$ (gauge invariance) and equal to half of the solid angle enclosed by the loop of spins on the unit sphere. In the continuum limit (infinitesimal small loops), this solid angle is proportional to the scalar spin chirality $\boldsymbol{n}_j \cdot \boldsymbol{n}_k \times \boldsymbol{n}_l$, which then acts as an effective magnetic field on the orbital degree of freedom of the conduction electrons [38].

In general, the spin-orbit interaction, which is always present in solids, modifies the above argument based on the scalar spin chirality. For example, a theoretical study of Mo oxides has proposed that the spin-orbit interaction significantly modifies the Hall conductivity of the noncoplanar phase, producing a much larger Hall effect in multiband systems [39]. However, to date, a systematic understanding of how the spin-orbit interaction modifies the geometric picture associated with the scalar spin chirality mechanism is lacking. The purpose of this paper is to derive the effective gauge field that emerges from a given magnetic texture *in the presence of finite SOC*. The SOC enters in the single-electron tight-binding Hamiltonian as a fixed SU(2) gauge field (defined on the lattice bonds) [40,41], whose value is determined by the interplay between the relativistic spin-orbit interaction and the crystal structure. We note that this field can fluctuate in theories where the ionic positions are allowed to fluctuate (e.g., theories that include electron-phonon coupling). In this work, we only include the electronic degrees of freedom, implying that the SU(2) gauge field remains frozen. The inclusion of finite SOC coupling in the hopping term of the *s-d* model leads to a more general form of the real-space Berry curvature (or effective magnetic field) in the double-exchange limit. In particular, it will become evident that noncoplanarity of the magnetic structure is no longer a requirement for producing a nontrivial real-space Berry curvature, i.e., collinear and coplanar structures can also produce an effective magnetic field in the presence of SOC. We will also see that the case of collinear ferromagnets that was originally considered by Karplus and Luttinger [10] is simply a limiting case of the general formula that we will derive here. Moreover, by taking the continuum limit of the model Hamiltonian under consideration, we derive an explicitly gauge-invariant form of the Berry curvature that generalizes the notion of scalar spin chirality. Finally, we consider a few simple examples to illustrate the applicability of these simple concepts to models and materials that exhibit topological Hall effect induced by coplanar and collinear magnetic orderings.

The presentation of our results is organized as follows. In Sec. II we formulate the general problem and we introduce the model Hamiltonian that will be used in the rest of the paper. Section III introduces a geometric approach for the computation of the electronic Berry phase in the presence of SOC. Mathematically oriented readers may find this approach more appealing than the algebraic treatment that is introduced in Sec. IV. However, the algebraic approach is probably more amenable for the general reader, who can skip Sec. III in a first reading of the paper. A similar consideration can be applied to the continuum limit of the theory that is described in Sec. V. While it is important to understand how the notion of scalar spin chirality [i.e., the source of the Berry curvature in the SU(2) invariant case] must be generalized in the presence of SOC, this is not a requirement for understanding the subsequent section, which is devoted to applying the generalized form of the real-space Berry curvature to simple lattice models. These simple models in Sec. VI capture the essence of the topological Hall effect that has been recently observed in materials with coplanar and collinear antiferromagnetic orderings, such as Mn_3Sn [42] and $CoNb_3S_6$ [43].

II. GENERAL FORMULATION

We will consider itinerant electrons that interact with localized magnetic moments via an exchange coupling J. For simplicity, we will assume that quantum fluctuations are small, implying the localized spins can be approximated by classical moments $\boldsymbol{S}_j = S\boldsymbol{n}_j$, where $\boldsymbol{n}_j$ is a normalized vector field

$$\boldsymbol{n}_j = (\sin\theta_j\cos\phi_j, \sin\theta_j\sin\phi_j, \cos\theta_j), \qquad (2)$$

representing the direction of the classical moment $\boldsymbol{S}_j$. In this classical limit, the sign of the exchange interaction J can be changed by the unitary transformation: $\boldsymbol{S}_j \to -\boldsymbol{S}_j$. Consequently, without loss of generality, we will adopt a ferromagnetic sign $J > 0$. The simplest Hamiltonian that describes this physics is

$$\mathcal{H} = \mathcal{H}_t + \mathcal{H}_J,$$
$$\mathcal{H}_t = \sum_{jk}(t_{kj}\boldsymbol{c}_k^\dagger U_{kj}\boldsymbol{c}_j + t_{kj}^*\boldsymbol{c}_j^\dagger U_{kj}^\dagger \boldsymbol{c}_k),$$
$$\mathcal{H}_J = -\frac{JS}{2}\sum_j \boldsymbol{c}_j^\dagger\boldsymbol{\sigma}\boldsymbol{c}_j \cdot \boldsymbol{n}_j. \qquad (3)$$

where $\boldsymbol{\sigma} = (\sigma_1, \sigma_2, \sigma_3)$ is a vector of the Pauli matrices. Here we are using the spinor notation

$$\boldsymbol{c}_k = \begin{bmatrix} c_{k\uparrow} \\ c_{k\downarrow} \end{bmatrix}, \quad \boldsymbol{c}_k^\dagger = [c_{k\uparrow}^\dagger \quad c_{k\downarrow}^\dagger]. \qquad (4)$$

The unitary operator U_{kj} is an SU(2) rotation matrix taking the general form

$$U_{kj} = \exp\left[-\frac{i\alpha_{kj}}{2}(\boldsymbol{a}_{kj}\cdot\boldsymbol{\sigma})\right], \qquad (5)$$

where α_{kj} is the rotation angle induced by the finite spin-orbit interaction, $\boldsymbol{a}_{kj}$ is the unit vector in the direction of the rotation axis. The complex hopping amplitudes t_{kj} can be expressed as $t_{kj} = |t_{kj}|e^{i\beta_{kj}}$. We note that $\mathcal{H}$ becomes SU(2) invariant in absence of SOC: $\alpha_{kj} = 0$ ($\forall\, kj$).

We will also assume that the exchange interaction J is comparable or larger than the bandwidth of the itinerant electrons. In this so-called double-exchange limit, the electronic spin orientation must remain parallel to the underlying localized spin. The resulting low-energy Hamiltonian is simply a spinless fermion tight-binding model with effective complex hopping amplitudes,

$$\tilde{t}_{kj} = \tau_{kj}e^{i\gamma_{kj}}, \qquad (6)$$

determined by the configuration of the underlying magnetic moments:

$$\tau_{kj} = t_{kj}\sqrt{\frac{1 + \boldsymbol{n}_k\cdot R_{kj}\cdot\boldsymbol{n}_j}{2}}. \qquad (7)$$

The SO(3) rotation matrix

$$R_{kj} = \exp[\alpha_{kj}(\boldsymbol{a}_{kj}\cdot\boldsymbol{L})] \qquad (8)$$

corresponds to the SU(2) rotation defined by the matrix U_{kj} in Eq. (5), where $\boldsymbol{L} = (L^x, L^y, L^z)$ is a vector of the standard SO(3) generators $[L^a]_{bc} = -\varepsilon^{abc}$. This is just a generalization of the Anderson-Hasegawa or double-exchange model to the case with finite SOC [36,37].

We are interested in the net phase Φ_{jkl} that the electronic wave function picks up as the electron moves around the triangle jkl. This phase is equal to the sum of two contributions:

$$\Phi_{jkl} = \beta_{jkl} + \gamma_{jkl}, \qquad (9)$$

where $\beta_{jkl} = \beta_{jl} + \beta_{lk} + \beta_{kj}$ is the phase that arises from the complex nature of the hopping amplitudes t_{kj}, which must be equal to 0 or π because $\mathcal{H}_t$ is time-reversal invariant. The Berry phase

$$\gamma_{jkl} = \gamma_{jl} + \gamma_{lk} + \gamma_{kj} \qquad (10)$$

arises from the strong exchange interaction between the electronic spin and the local moments, i.e., from the projection of the electronic spin state of each site j into the low-energy state:

$$|\boldsymbol{n}_j\rangle = \cos\frac{\theta_j}{2}|\uparrow\rangle + \sin\frac{\theta_j}{2}e^{i\phi_j}|\downarrow\rangle. \qquad (11)$$

While our requirement of adiabaticity is not necessary for generating a real-space Berry curvature, it greatly simplifies the analysis. In particular, it helps to identify the Berry curvature with a fictitious magnetic field that couples to the orbital motion of the itinerant electrons. In the absence of SOC, the flux of this effective magnetic field (in units of the flux quantum) through a closed loop is equal to half of the solid angle subtended by the local moments when moving around that loop. Correspondingly, in the long-wavelength limit, the fictitious magnetic field on a triangular plaquette jkl is proportional to the scalar product of the three local moments: $\boldsymbol{n}_j \cdot \boldsymbol{n}_k \times \boldsymbol{n}_l$.

In the presence of finite SOC, the Berry connection γ_{kj} becomes

$$\gamma_{kj} = \arg[\langle\boldsymbol{n}_k|U_{kj}|\boldsymbol{n}_j\rangle], \qquad (12)$$

where U_{kj} is the unitary operator in Eq. (5) describing the spin rotation as the electron hops from j to k. The goal of the next sections is to understand how this *extra spin rotation induced by finite SOC* modifies the effective magnetic field generated by the underlying vector field $\boldsymbol{n}$. Along this process, we will find an explicitly covariant expression for this effective magnetic field and we will learn that such a field can be nonzero for *collinear* and *coplanar* magnetic orderings, in addition to the noncoplanar orderings that are required for SU(2) invariant systems. We will see that this result unifies under a common frame the different magnetic orderings, such as collinear ferromagnetism and noncoplanar antiferromagnetism, that were previously identified as distinct potential sources of topological Hall effect.

III. GEOMETRIC APPROACH

A. Geodesic spin rotations

For any two spin states $|\boldsymbol{p}\rangle$ and $|\boldsymbol{q}\rangle$ corresponding to noncollinear unit vectors $\boldsymbol{p}$ and $\boldsymbol{q}$, we can define a "geodesic" SU(2) rotation $\tilde{U}_{\boldsymbol{q},\boldsymbol{p}}$ that rotates the spin direction from $\boldsymbol{p}$ to $\boldsymbol{q}$ along a geodesic (i.e., a great circle) of the Bloch sphere. If we choose the geodesic spin rotation to be along the shorter
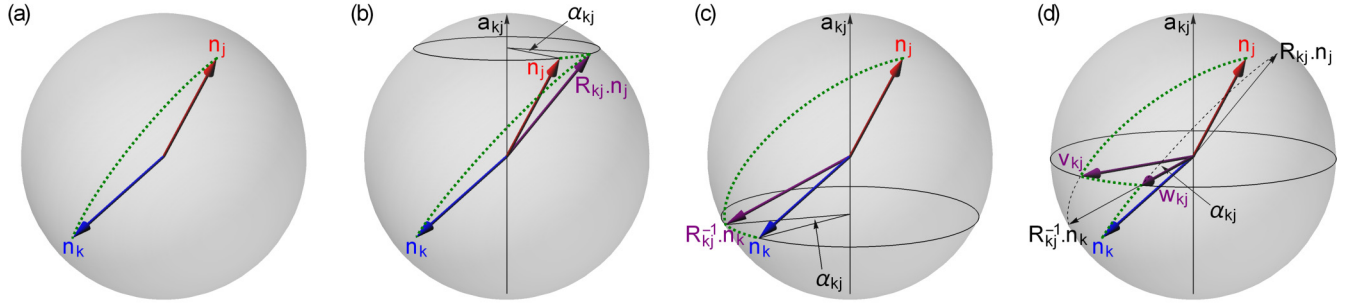
FIG. 1. (a) Great circle connecting the unit vectors $\boldsymbol{n}_j$ and $\boldsymbol{n}_k$. (b) The spin direction is first rotated around the axis $\boldsymbol{a}_{kj}$ and then along the great circle containing $R_{kj} \cdot \boldsymbol{n}_j$ and $\boldsymbol{n}_k$. (c) The spin direction is first rotated along the great circle containing $\boldsymbol{n}_j$ and $R_{kj}^{-1} \cdot \boldsymbol{n}_k$ and then around the axis $\boldsymbol{a}_{kj}$. (d) Unit vectors $\boldsymbol{v}_{kj}$ and $\boldsymbol{w}_{kj}$ along the great circle perpendicular to $\boldsymbol{a}_{kj}$. Using these two intermediate unit vectors, the spin rotation U_{kj} becomes a geodesic spin rotation $\tilde{U}_{\boldsymbol{w}_{kj}, \boldsymbol{v}_{kj}}$.

arc of the great circle containing both $\boldsymbol{p}$ and $\boldsymbol{q}$, it is unique and is given by

$$\tilde{U}_{\boldsymbol{q},\boldsymbol{p}} = \exp\left[-\frac{i\chi_{\boldsymbol{q},\boldsymbol{p}}}{2}(\boldsymbol{u}_{\boldsymbol{q},\boldsymbol{p}} \cdot \boldsymbol{\sigma})\right], \tag{13}$$

where the rotation angle $\chi_{\boldsymbol{q},\boldsymbol{p}} = \arccos(\boldsymbol{p} \cdot \boldsymbol{q}) < \pi$ is the angle between the two unit vectors $\boldsymbol{p}$ and $\boldsymbol{q}$, and the unit vector specifying the rotation axis is

$$\boldsymbol{u}_{\boldsymbol{q},\boldsymbol{p}} = \frac{\boldsymbol{p} \times \boldsymbol{q}}{|\boldsymbol{p} \times \boldsymbol{q}|} = \frac{\boldsymbol{p} \times \boldsymbol{q}}{\sin \chi_{\boldsymbol{q},\boldsymbol{p}}}. \tag{14}$$

It is instructive to consider the matrix element of this geodesic spin rotation $\tilde{U}_{\boldsymbol{q},\boldsymbol{p}}$ between the two spin states $|\boldsymbol{p}\rangle$ and $|\boldsymbol{q}\rangle$. By construction, $\tilde{U}_{\boldsymbol{q},\boldsymbol{p}}|\boldsymbol{p}\rangle \propto |\boldsymbol{q}\rangle$, and the geodesic matrix element $\langle \boldsymbol{q}|\tilde{U}_{\boldsymbol{q},\boldsymbol{p}}|\boldsymbol{p}\rangle$ is thus a complex number of unit modulus. To determine its complex argument, we first expand $\tilde{U}_{\boldsymbol{q},\boldsymbol{p}}$ in the standard way:

$$\langle \boldsymbol{q}|\tilde{U}_{\boldsymbol{q},\boldsymbol{p}}|\boldsymbol{p}\rangle = \langle \boldsymbol{q}|\left[\cos \frac{\chi_{\boldsymbol{q},\boldsymbol{p}}}{2} - i(\boldsymbol{u}_{\boldsymbol{q},\boldsymbol{p}} \cdot \boldsymbol{\sigma})\sin \frac{\chi_{\boldsymbol{q},\boldsymbol{p}}}{2}\right]|\boldsymbol{p}\rangle$$

$$= \cos \frac{\chi_{\boldsymbol{q},\boldsymbol{p}}}{2} \langle \boldsymbol{q}|\boldsymbol{p}\rangle$$

$$- \frac{i}{2}\left[\cos \frac{\chi_{\boldsymbol{q},\boldsymbol{p}}}{2}\right]^{-1} \langle \boldsymbol{q}|[(\boldsymbol{p} \times \boldsymbol{q}) \cdot \boldsymbol{\sigma}]|\boldsymbol{p}\rangle. \tag{15}$$

With some straightforward algebra, it can then be shown that the matrix element in the second term of Eq. (15) is proportional to the overlap in the first term:

$$\langle \boldsymbol{q}|[(\boldsymbol{p} \times \boldsymbol{q}) \cdot \boldsymbol{\sigma}]|\boldsymbol{p}\rangle = 2i \sin^2 \frac{\chi_{\boldsymbol{q},\boldsymbol{p}}}{2} \langle \boldsymbol{q}|\boldsymbol{p}\rangle. \tag{16}$$

Using this relation, the geodesic matrix element in Eq. (15) can be written as

$$\langle \boldsymbol{q}|\tilde{U}_{\boldsymbol{q},\boldsymbol{p}}|\boldsymbol{p}\rangle = \left[\cos \frac{\chi_{\boldsymbol{q},\boldsymbol{p}}}{2}\right]^{-1} \langle \boldsymbol{q}|\boldsymbol{p}\rangle = \frac{\langle \boldsymbol{q}|\boldsymbol{p}\rangle}{|\langle \boldsymbol{q}|\boldsymbol{p}\rangle|}. \tag{17}$$

Since $|\langle \boldsymbol{q}|\boldsymbol{p}\rangle|$ is real and positive by definition, the argument of the geodesic matrix element $\langle \boldsymbol{q}|\tilde{U}_{\boldsymbol{q},\boldsymbol{p}}|\boldsymbol{p}\rangle$ is identical to the argument of the overlap $\langle \boldsymbol{q}|\boldsymbol{p}\rangle$.

B. SU(2) invariant case

If the electron spin is not rotated as it hops between different sites of the triangle, the Berry connection in Eq. (12)

takes the simplified form

$$\gamma_{kj} = \arg[\langle \boldsymbol{n}_k|\boldsymbol{n}_j\rangle]. \tag{18}$$

Employing Eq. (17) to turn the overlap in Eq. (18) into a geodesic matrix element, this Berry connection can be written as

$$\gamma_{kj} = \arg\left[\langle \boldsymbol{n}_k|\tilde{U}_{\boldsymbol{n}_k,\boldsymbol{n}_j}|\boldsymbol{n}_j\rangle\right] = \arg\left[\langle \boldsymbol{n}_k|\left(\tilde{U}_{\boldsymbol{n}_k,\boldsymbol{n}_j}^{1/N}\right)^N|\boldsymbol{n}_j\rangle\right]$$

$$= \arg\left[\langle \boldsymbol{n}_k|\tilde{U}_{\boldsymbol{n}_k,\boldsymbol{n}_{kj}^{(N-1)}} \dots \tilde{U}_{\boldsymbol{n}_{kj}^{(2)},\boldsymbol{n}_{kj}^{(1)}}\tilde{U}_{\boldsymbol{n}_{kj}^{(1)},\boldsymbol{n}_j}|\boldsymbol{n}_j\rangle\right], \tag{19}$$

where $N \to \infty$ is a large number, and $\boldsymbol{n}_{kj}^{(n)}$ in terms of $n = 1, 2, \dots, N-1$ are unit vectors equally spaced along the great circle connecting $\boldsymbol{n}_j$ and $\boldsymbol{n}_k$ [see Fig. 1(a)]. At the intermediate step between the infinitesimal spin rotations $\tilde{U}_{\boldsymbol{n}_{kj}^{(n)},\boldsymbol{n}_{kj}^{(n-1)}}$ and $\tilde{U}_{\boldsymbol{n}_{kj}^{(n+1)},\boldsymbol{n}_{kj}^{(n)}}$ in Eq. (19), the spin state is proportional to $|\boldsymbol{n}_{kj}^{(n)}\rangle$ by construction. If we then use the orthogonality relation $\langle -\boldsymbol{p}|\boldsymbol{p}\rangle = 0$ and the resolution of identity

$$|\boldsymbol{p}\rangle\langle\boldsymbol{p}| + |-\boldsymbol{p}\rangle\langle-\boldsymbol{p}| = 1 \tag{20}$$

for $|\boldsymbol{p}\rangle = |\boldsymbol{n}_{kj}^{(n)}\rangle$ at each intermediate step, and also Eq. (17) to turn each geodesic matrix element back into an overlap, the Berry connection in Eq. (19) becomes

$$\gamma_{kj} = \arg\left[\langle \boldsymbol{n}_k|\tilde{U}_{\boldsymbol{n}_k,\boldsymbol{n}_{kj}^{(N-1)}}|\boldsymbol{n}_{kj}^{(N-1)}\rangle \dots\right.$$

$$\left.\langle \boldsymbol{n}_{kj}^{(2)}|\tilde{U}_{\boldsymbol{n}_{kj}^{(2)},\boldsymbol{n}_{kj}^{(1)}}|\boldsymbol{n}_{kj}^{(1)}\rangle\langle \boldsymbol{n}_{kj}^{(1)}|\tilde{U}_{\boldsymbol{n}_{kj}^{(1)},\boldsymbol{n}_j}|\boldsymbol{n}_j\rangle\right]$$

$$= \arg\left[\langle \boldsymbol{n}_k|\boldsymbol{n}_{kj}^{(N-1)}\rangle\right] + \dots + \arg\left[\langle \boldsymbol{n}_{kj}^{(2)}|\boldsymbol{n}_{kj}^{(1)}\rangle\right]$$

$$+ \arg\left[\langle \boldsymbol{n}_{kj}^{(1)}|\boldsymbol{n}_j\rangle\right]. \tag{21}$$

Consequently, the Berry phase in Eq. (10) is a sum of infinitely many infinitesimal Berry connections along a closed loop in the Hilbert space and can thus be converted into an appropriate integral of the Berry curvature along a surface bounded by this closed loop. For spin states, it is well known that the Berry curvature is $\frac{1}{2}$ everywhere on the Bloch sphere, and the Berry phase γ_{jkl} in Eq. (10) is therefore half the solid angle of the spherical triangle spanned by $\boldsymbol{n}_j$, $\boldsymbol{n}_k$, and $\boldsymbol{n}_l$.

C. General case with spin-orbit interaction

To calculate the general Berry connection in Eq. (12), we first notice that $U_{kj}|\boldsymbol{n}_j\rangle \propto |R_{kj} \cdot \boldsymbol{n}_j\rangle$. Using Eq. (20) for $|\boldsymbol{p}\rangle = |R_{kj} \cdot \boldsymbol{n}_j\rangle$, the Berry connection in Eq. (12) then becomes

$$\gamma_{kj} = \arg[\langle \boldsymbol{n}_k | R_{kj} \cdot \boldsymbol{n}_j \rangle \langle R_{kj} \cdot \boldsymbol{n}_j | U_{kj} | \boldsymbol{n}_j \rangle]. \quad (22)$$

Next, if we employ Eq. (17) to turn the overlap into a geodesic matrix element, and use Eq. (20) with $|\boldsymbol{p}\rangle = |R_{kj} \cdot \boldsymbol{n}_j\rangle$ again, the Berry connection takes the form

$$\gamma_{kj} = \arg[\langle \boldsymbol{n}_k | \tilde{U}_{\boldsymbol{n}_k, R_{kj} \cdot \boldsymbol{n}_j} | R_{kj} \cdot \boldsymbol{n}_j \rangle \langle R_{kj} \cdot \boldsymbol{n}_j | U_{kj} | \boldsymbol{n}_j \rangle]$$
$$= \arg[\langle \boldsymbol{n}_k | \tilde{U}_{\boldsymbol{n}_k, R_{kj} \cdot \boldsymbol{n}_j} U_{kj} | \boldsymbol{n}_j \rangle]. \quad (23)$$

In this representation, the spin direction is first rotated around the axis $\boldsymbol{a}_{kj}$ and then along the great circle containing $R_{kj} \cdot \boldsymbol{n}_j$ and $\boldsymbol{n}_k$ [see Fig. 1(b)]. By exploiting the identity

$$U_{kj}^{-1} \tilde{U}_{\boldsymbol{n}_k, R_{kj} \cdot \boldsymbol{n}_j} U_{kj} = \tilde{U}_{R_{kj}^{-1} \cdot \boldsymbol{n}_k, \boldsymbol{n}_j}, \quad (24)$$

we can also obtain an alternative formula for the Berry connection:

$$\gamma_{kj} = \arg\left[\langle \boldsymbol{n}_k | U_{kj} \tilde{U}_{R_{kj}^{-1} \cdot \boldsymbol{n}_k, \boldsymbol{n}_j} | \boldsymbol{n}_j \rangle\right]. \quad (25)$$

In this representation, the spin direction is first rotated along the great circle containing $\boldsymbol{n}_j$ and $R_{kj}^{-1} \cdot \boldsymbol{n}_k$ and then around the axis $\boldsymbol{a}_{kj}$ [see Fig. 1(c)]. Generically, in either of these two representations, the rotation around the axis $\boldsymbol{a}_{kj}$ is *not* along a great circle of the Bloch sphere. However, there is a "mixed" representation between these two "pure" representations in which the spin direction is rotated along great circles all the way from $\boldsymbol{n}_j$ to $\boldsymbol{n}_k$: first along the one containing $\boldsymbol{n}_j$ and $R_{kj}^{-1} \cdot \boldsymbol{n}_k$, then along the one perpendicular to $\boldsymbol{a}_{kj}$, and finally along the one containing $R_{kj} \cdot \boldsymbol{n}_j$ and $\boldsymbol{n}_k$. To find the corresponding formula for the Berry connection, we start from Eq. (25) and notice that there is a general identity

$$U_{kj} \tilde{U}_{R_{kj}^{-1} \cdot \boldsymbol{n}_k, \boldsymbol{n}_j} = \pm U_{kj} \tilde{U}_{R_{kj}^{-1} \cdot \boldsymbol{n}_k, \boldsymbol{v}_{kj}} \tilde{U}_{\boldsymbol{v}_{kj}, \boldsymbol{n}_j}$$
$$= \pm \tilde{U}_{\boldsymbol{n}_k, R_{kj} \cdot \boldsymbol{v}_{kj}} U_{kj} \tilde{U}_{\boldsymbol{v}_{kj}, \boldsymbol{n}_j} \quad (26)$$

for any unit vector $\boldsymbol{v}_{kj}$ along the great circle containing $\boldsymbol{n}_j$ and $R_{kj}^{-1} \cdot \boldsymbol{n}_k$. The sign ambiguity in Eq. (26) reflects that the left-hand side and the right-hand side may differ in a 2π spin rotation $e^{i\pi} = -1$. We ignore this sign ambiguity as it does not matter for our purposes. Next, if the unit vector $\boldsymbol{v}_{kj}$ is also along the great circle perpendicular to $\boldsymbol{a}_{kj}$ [see Fig. 1(d)], the spin rotation U_{kj} becomes a geodesic spin rotation $\tilde{U}_{\boldsymbol{w}_{kj}, \boldsymbol{v}_{kj}}$, where $\boldsymbol{w}_{kj} = R_{kj} \cdot \boldsymbol{v}_{kj}$, and thus Eq. (26) takes the form

$$U_{kj} \tilde{U}_{R_{kj}^{-1} \cdot \boldsymbol{n}_k, \boldsymbol{n}_j} = \pm \tilde{U}_{\boldsymbol{n}_k, \boldsymbol{w}_{kj}} \tilde{U}_{\boldsymbol{w}_{kj}, \boldsymbol{v}_{kj}} \tilde{U}_{\boldsymbol{v}_{kj}, \boldsymbol{n}_j}. \quad (27)$$

The unit vector $\boldsymbol{v}_{kj}$ is then along the intersection of the great circle perpendicular to $\boldsymbol{a}_{kj}$ and the great circle containing $\boldsymbol{n}_j$ and $R_{kj}^{-1} \cdot \boldsymbol{n}_k$:

$$\boldsymbol{v}_{kj} = \frac{\boldsymbol{a}_{kj} \times [\boldsymbol{n}_j \times (R_{kj}^{-1} \cdot \boldsymbol{n}_k)]}{|\boldsymbol{a}_{kj} \times [\boldsymbol{n}_j \times (R_{kj}^{-1} \cdot \boldsymbol{n}_k)]|}, \quad (28)$$

while the unit vector $\boldsymbol{w}_{kj}$ is along the intersection of the great circle perpendicular to $\boldsymbol{a}_{kj}$ and the great circle containing $R_{kj} \cdot$

$\boldsymbol{n}_j$ and $\boldsymbol{n}_k$:

$$\boldsymbol{w}_{kj} = R_{kj} \cdot \boldsymbol{v}_{kj} = \frac{\boldsymbol{a}_{kj} \times [(R_{kj} \cdot \boldsymbol{n}_j) \times \boldsymbol{n}_k]}{|\boldsymbol{a}_{kj} \times [(R_{kj} \cdot \boldsymbol{n}_j) \times \boldsymbol{n}_k]|}. \quad (29)$$

Note that $-\boldsymbol{v}_{kj}$ and $-\boldsymbol{w}_{kj}$ are also along the intersections of the same great circles and could thus be used instead of $\boldsymbol{v}_{kj}$ and $\boldsymbol{w}_{kj}$ in Eq. (27). Substituting Eq. (27) into Eq. (25), and using Eqs. (17) and (20), the Berry connection finally becomes

$$\gamma_{kj} = \arg\left[\pm \langle \boldsymbol{n}_k | \tilde{U}_{\boldsymbol{n}_k, \boldsymbol{w}_{kj}} \tilde{U}_{\boldsymbol{w}_{kj}, \boldsymbol{v}_{kj}} \tilde{U}_{\boldsymbol{v}_{kj}, \boldsymbol{n}_j} | \boldsymbol{n}_j \rangle\right]$$
$$= \arg\left[\pm \langle \boldsymbol{n}_k | \tilde{U}_{\boldsymbol{n}_k, \boldsymbol{w}_{kj}} | \boldsymbol{w}_{kj} \rangle \langle \boldsymbol{w}_{kj} | \tilde{U}_{\boldsymbol{w}_{kj}, \boldsymbol{v}_{kj}} | \boldsymbol{v}_{kj} \rangle \langle \boldsymbol{v}_{kj} | \tilde{U}_{\boldsymbol{v}_{kj}, \boldsymbol{n}_j} | \boldsymbol{n}_j \rangle\right]$$
$$= \arg[\langle \boldsymbol{n}_k | \boldsymbol{w}_{kj} \rangle] + \arg[\langle \boldsymbol{w}_{kj} | \boldsymbol{v}_{kj} \rangle]$$
$$+ \arg[\langle \boldsymbol{v}_{kj} | \boldsymbol{n}_j \rangle] \quad (\mathrm{mod}\ \pi).$$

Consequently, the Berry phase is a sum of nine Berry connections, each taking the simplified form of Eq. (18). Repeating the steps of Sec. III B, the Berry phase γ_{jkl} in Eq. (10) is then half the solid angle of the spherical *nonagon* spanned by $\boldsymbol{n}_j$, $\boldsymbol{v}_{kj}, \boldsymbol{w}_{kj}, \boldsymbol{n}_k, \boldsymbol{v}_{lk}, \boldsymbol{w}_{lk}, \boldsymbol{n}_l, \boldsymbol{v}_{jl},$ and $\boldsymbol{w}_{jl}$. While this result is only valid modulo π, it can be used to deduce if the effective flux produced by the combination of magnetic ordering and SOC breaks the time-reversal symmetry or not.

The most important consequence of this result is that the Berry curvature (i.e., the effective magnetic field) can be nonzero even for *collinear* or *coplanar* spin configurations if the spin-orbit interaction is finite. This feature will become clearer in the next section, where we solve the same problem by using a convenient rotation of the local reference frame at each individual spin.

IV. ALGEBRAIC APPROACH

A. SU(2) invariant case

We have seen in the previous section that, in absence of spin-orbit coupling, the Berry phase γ_{jkl} picked up by an electron as it moves around a triangle of spins jkl is half the solid angle subtended by the three spins:

$$\gamma_{jkl} = \frac{\Omega_{jkl}}{2}. \quad (30)$$

This simple equation can be rederived in the following way. We first introduce an arbitrary unit vector $\boldsymbol{n}$ that we choose as our quantization axis, i.e., $\boldsymbol{n} = \hat{z}$. In this frame, the states of the spins j and k are

$$|\boldsymbol{n}_j\rangle = \cos\frac{\theta_j}{2}|\uparrow\rangle + e^{i\phi_j}\sin\frac{\theta_j}{2}|\downarrow\rangle,$$
$$|\boldsymbol{n}_k\rangle = \cos\frac{\theta_k}{2}|\uparrow\rangle + e^{i\phi_k}\sin\frac{\theta_k}{2}|\downarrow\rangle. \quad (31)$$

Given that $\phi_j - \phi_k$ is defined modulo 2π, we will use this freedom to require that $|\phi_j - \phi_k| \leqslant \pi$. In absence of SOC, the Berry connection becomes

$$\gamma_{kj} = \arg[\langle \boldsymbol{n}_k | \boldsymbol{n}_j \rangle]$$
$$= \arg\left[\cos\frac{\theta_j}{2}\cos\frac{\theta_k}{2} + e^{i(\phi_j - \phi_k)}\sin\frac{\theta_j}{2}\sin\frac{\theta_k}{2}\right], \quad (32)$$

implying that

$$\tan \gamma_{kj} = \frac{\sin (\phi_j - \phi_k)}{\cot \frac{\theta_j}{2} \cot \frac{\theta_k}{2} + \cos (\phi_j - \phi_k)}$$

$$= \tan \frac{\Omega(\phi_j - \phi_k, \theta_j, \theta_k)}{2}, \qquad (33)$$

where $\Omega(\phi_j - \phi_k, \theta_j, \theta_k)$ is the solid angle subtended by the vectors $(\boldsymbol{n}, \boldsymbol{n}_j, \boldsymbol{n}_k)$. Since the quantization axis $\boldsymbol{n}$ is the same for the three bonds of the triangle, the Berry phase is indeed given by Eq. (30):

$$\gamma_{jkl} = \gamma_{kj} + \gamma_{lk} + \gamma_{jl} = \frac{\Omega_{jkl}}{2}, \qquad (34)$$

where Ω_{jkl} is the solid angle subtended by the vectors $(\boldsymbol{n}_j, \boldsymbol{n}_k, \boldsymbol{n}_l)$ corresponding to the spin directions.

B. General case with spin-orbit interaction

Our next goal is to generalize Eq. (34) for the case of finite SOC, where

$$\gamma_{jkl} = \arg[\langle \boldsymbol{n}_k | U_{kj} | \boldsymbol{n}_j \rangle \langle \boldsymbol{n}_l | U_{lk} | \boldsymbol{n}_k \rangle \langle \boldsymbol{n}_j | U_{jl} | \boldsymbol{n}_l \rangle]. \qquad (35)$$

We first notice that the Berry phase γ_{jkl} is invariant under local rotations of the spin reference frame,

$$|\boldsymbol{n}_j'\rangle = \mathcal{U}_j |\boldsymbol{n}_j\rangle, \quad |\boldsymbol{n}_k'\rangle = \mathcal{U}_k |\boldsymbol{n}_k\rangle, \quad |\boldsymbol{n}_l'\rangle = \mathcal{U}_l |\boldsymbol{n}_l\rangle, \quad (36)$$

$$\boldsymbol{n}_j' = \mathcal{R}_j \cdot \boldsymbol{n}_j, \quad \boldsymbol{n}_k' = \mathcal{R}_k \cdot \boldsymbol{n}_k, \quad \boldsymbol{n}_l' = \mathcal{R}_l \cdot \boldsymbol{n}_l, \quad (37)$$

where $\mathcal{R}_j$ is the SO(3) rotation matrix associated with the SU(2) matrix $\mathcal{U}_j$, if we simultaneously transform the unitary operator on each bond in the following way:

$$U_{kj}' = \mathcal{U}_k U_{kj} \mathcal{U}_j^\dagger, \quad U_{lk}' = \mathcal{U}_l U_{lk} \mathcal{U}_k^\dagger, \quad U_{jl}' = \mathcal{U}_j U_{jl} \mathcal{U}_l^\dagger. \quad (38)$$

This observation simply reflects the gauge invariance of the Berry phase under rotations of the local spin reference frame and it motivates the introduction of the Wilson loop operator

$$\mathcal{A}_{jkl} = U_{jl} U_{lk} U_{kj} = \exp \left[-\frac{i\alpha_{jkl}}{2} (\boldsymbol{a}_{jkl} \cdot \boldsymbol{\sigma}) \right], \qquad (39)$$

which is also a gauge-invariant quantity. We note that the exchange Hamiltonian $\mathcal{H}_J$ between the spins of the itinerant electrons and the local magnetic moments remains invariant under the local spin rotations described by Eqs. (36) and (37).

The next step is to perform a convenient rotation of the local reference frame of two spins (say k and l) such that the unitary operator becomes the identity on two out of three bonds (say kj and jl). To this end, one can use the local unitary transformations

$$\mathcal{U}_j = I, \quad \mathcal{U}_k = U_{kj}^\dagger, \quad \mathcal{U}_l = U_{jl},$$

$$\mathcal{R}_j = I, \quad \mathcal{R}_k = R_{kj}^T, \quad \mathcal{R}_l = R_{jl}. \qquad (40)$$

Given that the Wilson loop remains invariant under such a transformation, the unitary operator on the third bond lk must then be equal to the Wilson loop $\mathcal{A}_{jkl}$.

The final step is to align the global quantization axis $\boldsymbol{n}$ with the rotation axis of the Wilson loop operator: $\boldsymbol{n} = \boldsymbol{a}_{jkl}$. The

Berry connections can then be easily computed in the new reference frame:

$$\gamma_{kj} = \arg[\langle \boldsymbol{n}_k' | \boldsymbol{n}_j' \rangle] = \frac{\Omega(\phi_j' - \phi_k', \theta_j', \theta_k')}{2},$$

$$\gamma_{jl} = \arg[\langle \boldsymbol{n}_j' | \boldsymbol{n}_l' \rangle] = \frac{\Omega(\phi_l' - \phi_j', \theta_l', \theta_j')}{2},$$

$$\gamma_{lk} = \arg[\langle \boldsymbol{n}_l' | \mathcal{A}_{jkl} | \boldsymbol{n}_k' \rangle]$$

$$= \arg \left[e^{-\frac{i}{2}\alpha_{jkl}} \cos \frac{\theta_k'}{2} \cos \frac{\theta_l'}{2} + e^{i(\phi_k' - \phi_l' + \frac{1}{2}\alpha_{jkl})} \sin \frac{\theta_k'}{2} \sin \frac{\theta_l'}{2} \right]$$

$$= -\frac{\alpha_{jkl}}{2} + \frac{\Omega(\phi_k' - \phi_l' + \alpha_{jkl}, \theta_k', \theta_l')}{2}. \qquad (41)$$

Thus, the Berry phase picked up by an electron as it moves around the triangle jkl is

$$\gamma_{jkl} = \frac{\Omega_{jkl}'}{2} + \hat{\gamma}_{jkl}, \qquad (42)$$

where Ω_{jkl}' is the solid angle subtended by the three vectors $(\boldsymbol{n}_j', \boldsymbol{n}_k', \boldsymbol{n}_l')$ corresponding to the rotated spin directions in the new reference frame, and

$$\hat{\gamma}_{jkl} = -\frac{\alpha_{jkl}}{2} + \frac{\delta \Omega_{jkl}'}{2}, \qquad (43)$$

in terms of

$$\delta \Omega_{jkl}' = \Omega(\phi_k' - \phi_l' + \alpha_{jkl}, \theta_k', \theta_l') - \Omega(\phi_k' - \phi_l', \theta_k', \theta_l'), \qquad (44)$$

is an additional contribution due to the Wilson loop $\mathcal{A}_{jkl}$.

Equation (42) generalizes Eq. (30), which is only valid for SU(2) invariant systems. In particular, it is easy to demonstrate that collinear or coplanar configurations can induce a Berry phase different from 0 or π, which acts as an effective magnetic flux. As an example, we can consider the case of a collinear ferromagnet $\boldsymbol{n}_j \parallel \boldsymbol{n}_k \parallel \boldsymbol{n}_j$ with the three vectors $\boldsymbol{a}_{kj}$, $\boldsymbol{a}_{lk}$, and $\boldsymbol{a}_{jl}$ being parallel (or antiparallel) to the magnetization. In this case, Eq. (42) tells us that that $\gamma_{jkl} = -\alpha_{jkl}/2$, implying that the combination of ferromagnetism and SOC generates a real-space Berry phase that is proportional to the rotation angle of the Wilson loop. In this way, we recover the essential result of Karplus and Luttinger [10] in the minimal model that we are considering here. The potential emergence of real-space Berry curvature in coplanar antiferromagnets will become clearer in the next section, where we discuss the limit of small SOC. However, one can immediately verify that Eq. (42) also gives a finite Berry curvature for the coplanar spin configuration illustrated in Fig. 2.

C. Limit of small spin-orbit interaction

We will now consider the quite general case of small spin-orbit coupling: $\alpha_{kj} \ll 1$ for all bonds kj connected by finite hopping amplitudes t_{kj} (the hopping amplitudes are assumed to be zero beyond a characteristic distance of a few lattice spaces because of the exponential decay of the atomic orbitals). Expanding Eqs. (5) and (39) up to first order in α_{kj} and α_{jkl}, respectively, the parameters of the Wilson loop operator then easily follow from those of the individual
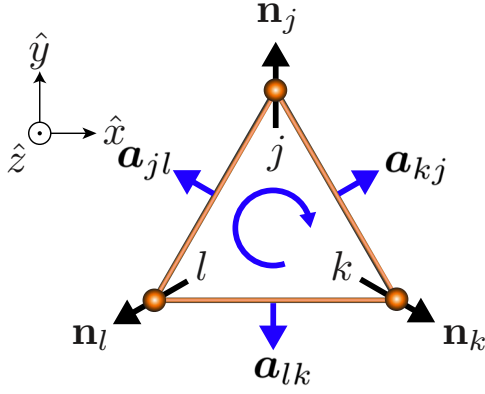
FIG. 2. Coplanar configuration with Berry phase different from 0 or π. The clockwise circulation indicates the bond orientations required to define the directions of the spin-orbit vectors $\boldsymbol{a}_{kj}$, $\boldsymbol{a}_{lk}$, and $\boldsymbol{a}_{jl}$, indicated with blue arrows.

unitary operators:

$$\alpha_{jkl} = |\boldsymbol{v}_{jkl}|, \qquad \boldsymbol{a}_{jkl} = \frac{\boldsymbol{v}_{jkl}}{|\boldsymbol{v}_{jkl}|},$$

$$\boldsymbol{v}_{jkl} = \alpha_{kj}\boldsymbol{a}_{kj} + \alpha_{lk}\boldsymbol{a}_{lk} + \alpha_{jl}\boldsymbol{a}_{jl}. \tag{45}$$

Moreover, the contribution to the Berry phase in Eq. (43) can be expanded up to first order in α_{jkl} as

$$\hat{\gamma}_{jkl} = \frac{\alpha_{jkl}}{2}\left[-1 + \frac{\partial\Omega(\phi'_k - \phi'_l + \alpha, \theta'_k, \theta'_l)}{\partial\alpha}\bigg|_{\alpha=0}\right], \tag{46}$$

and can be brought to a simple form via Eq. (33):

$$\hat{\gamma}_{jkl} = -\frac{\alpha_{jkl}(\cos\theta'_k + \cos\theta'_l)}{2[1 + \cos\theta'_k \cos\theta'_l + \sin\theta'_k \sin\theta'_l \cos(\phi'_k - \phi'_l)]}. \tag{47}$$

In particular, when the spin directions are close to a ferromagnetic configuration, such that $\theta'_k \approx \theta'_l \approx \theta'$ and $\phi'_k \approx \phi'_l \approx \phi'$, this contribution becomes

$$\hat{\gamma}_{jkl} = -\frac{\alpha_{jkl}\cos\theta'}{2}, \tag{48}$$

which is simply *the projection of the net spin-orbit rotation to the common direction of the spins*.

In the special case when the Wilson loop is equal to the identity ($\alpha_{jkl} = 0$), the Berry phase $\hat{\gamma}_{jkl}$ in Eq. (43) vanishes. The total Berry phase γ_{jkl} in Eq. (42) is then half the solid angle Ω'_{jkl} subtended by the three magnetic moments *in the local reference frame* that is required to "gauge away" the SOC. Clearly, even in this case, an antiferromagnetic ordering that is coplanar in the original reference frame can be non-coplanar in the rotated reference frame and thus produce a finite real-space Berry curvature.

For example, in the C_3 invariant system depicted in Fig. 2, the three angles $\alpha_{kj} = \alpha_{lk} = \alpha_{jl} = \alpha \ll 1$ are identical, and the three vectors $\boldsymbol{a}_{kj}$, $\boldsymbol{a}_{lk}$, and $\boldsymbol{a}_{jl}$ are related by $2\pi/3$ rotations around the $\hat{z}$ axis. Consequently,

$$\boldsymbol{v}_{jkl} = \alpha(\boldsymbol{a}_{kj} + \boldsymbol{a}_{lk} + \boldsymbol{a}_{jl}) = 0 \tag{49}$$

if the z component of $\boldsymbol{a}_{kj}$ vanishes. In other words, to first order in the SOC, the Wilson loop is equal to the identity:

$\mathcal{A}_{jkl} = I$. To the same order, the three spin directions in the new reference frame are

$$\boldsymbol{n}'_j = \boldsymbol{n}_j, \quad \boldsymbol{n}'_k = \boldsymbol{n}_k - \alpha\boldsymbol{a}_{kj}\times\boldsymbol{n}_k, \quad \boldsymbol{n}'_l = \boldsymbol{n}_l + \alpha\boldsymbol{a}_{jl}\times\boldsymbol{n}_l, \tag{50}$$

and the Berry phase is thus given by

$$\gamma_{jkl} = \frac{\Omega'_{jkl}}{2} = \pi - 6\alpha + \mathcal{O}(\alpha^2). \tag{51}$$

The simple message of this example is that, whenever the SOC can be gauged away in a particular local reference frame (i.e., the Wilson loop is equal to the identity), *the magnetic ordering must be noncoplanar in that reference frame to produce a finite real-space Berry curvature*. It is easy to imagine that antiferromagnetic orderings that are collinear or coplanar in the original reference frame can become noncoplanar in the rotated reference frame leading to a finite Berry curvature.

V. CONTINUUM LIMIT

The simple ideas that we discussed in the previous section can be presented in a more formal and elegant way by taking the continuum limit. This limit is appropriate for describing situations where the SU(2) Wilson loop bond field defined by $\mathcal{A}_{jkl}$, associated with the SOC, and the magnetic texture vary over a length scale which is much longer than the lattice parameter. The first condition can be realized by long-wavelength lattice deformations induced by strain. The second condition arises naturally in materials with a very small magnetic ordering wave vector.

By taking the continuum limit, we will find an explicitly covariant form of the effective magnetic field or real-space Berry curvature produced by the underlying vector field $\boldsymbol{n}_j$ in presence of SOC. We have seen that the unitary "hopping" matrices U_{jk} correspond to a non-Abelian SU(2) gauge field which is fixed by the interplay between the lattice structure and the SOC.[1] After taking the continuum limit, the bond matrices U_{jk} become infinitesimal SU(2) rotations connecting the points $\boldsymbol{x}$ and $\boldsymbol{x} + d\boldsymbol{x}$ which are parametrized by the field A^a_μ:

$$U_{\boldsymbol{x}+d\boldsymbol{x},\boldsymbol{x}} = \exp\left[\frac{1}{2}\sigma^a A^a_\mu dx_\mu\right], \tag{52}$$

where repeated indices are implicitly summed over.

Once again, we want to compute the Berry phase that the electronic wave function acquires when the electron moves along a one-dimensional closed path $\mathcal{C} = \{x_\mu(\tau) \text{ with } \tau \in [0; T], x_\mu(0) = x_\mu(T)\}$. As we did for the lattice case, we will first derive the well-known expression of the Berry phase in the SU(2) invariant case and we will use this result as an introduction for obtaining a gauge-invariant form of the Berry curvature or effective magnetic field in the presence of SOC.

A. SU(2) invariant case

For the SU(2) invariant case on the lattice, we have seen that the Berry phase for a closed loop $\mathcal{C}: j \to k \to l \to$

---

[1]This field becomes a dynamical variable if the ionic positions are allowed to fluctuate.

$\cdots \to m \to j$ is

$$\gamma_\mathcal{C} = \arg[\langle \boldsymbol{n}_j | \boldsymbol{n}_m \rangle \ldots \langle \boldsymbol{n}_l | \boldsymbol{n}_k \rangle \langle \boldsymbol{n}_k | \boldsymbol{n}_j \rangle]. \qquad (53)$$

Note that an arbitrary closed loop can be obtained from a superposition of multiple "elementary" triangular loops. To find the counterpart of Eq. (53) in the continuum, we will divide the interval T into N equal subintervals $\Delta\tau = T/N$ to finally take the $N \to \infty$ limit. In this way we obtain

$$\gamma_\mathcal{C} = \lim_{N\to\infty} \arg \left\{ \prod_{j=0}^{N-1} \langle \boldsymbol{n}_{\boldsymbol{x}(\tau_j + \Delta\tau)} | \boldsymbol{n}_{\boldsymbol{x}(\tau_j)} \rangle \right\}$$

$$= \lim_{N\to\infty} \arg \left\{ \prod_{j=0}^{N-1} [1 - \langle \boldsymbol{n}_{\boldsymbol{x}(\tau_j)} | \partial_\tau | \boldsymbol{n}_{\boldsymbol{x}(\tau_j)} \rangle \Delta\tau] \right\}$$

$$= \lim_{N\to\infty} \arg \left\{ \prod_{j=0}^{N-1} \exp [-\langle \boldsymbol{n}_{\boldsymbol{x}(\tau_j)} | \partial_\tau | \boldsymbol{n}_{\boldsymbol{x}(\tau_j)} \rangle \Delta\tau] \right\}$$

$$= i \lim_{N\to\infty} \sum_{j=0}^{N-1} \langle \boldsymbol{n}_{\boldsymbol{x}(\tau_j)} | \partial_\tau | \boldsymbol{n}_{\boldsymbol{x}(\tau_j)} \rangle \Delta\tau$$

$$= i \int_0^T \langle \boldsymbol{n}_{\boldsymbol{x}(\tau)} | \partial_\tau | \boldsymbol{n}_{\boldsymbol{x}(\tau)} \rangle d\tau, \qquad (54)$$

where $\tau_j = j\Delta\tau$. The geometric character of the Berry phase becomes evident after reexpressing Eq. (54) in terms of a closed integral over the loop $\mathcal{C}$:

$$\gamma_\mathcal{C} = i \oint_\mathcal{C} \langle \boldsymbol{n} | \partial_\mu | \boldsymbol{n} \rangle dx_\mu = \frac{1}{2} \int_{S_\mathcal{C}} \boldsymbol{n} \cdot [\partial_\mu \boldsymbol{n} \times \partial_\nu \boldsymbol{n}] d^2\sigma^{\mu\nu} = \frac{\Omega_\mathcal{C}}{2}, \qquad (55)$$

where $S_\mathcal{C}$ is the area enclosed by the loop $\mathcal{C}$, while $\Omega_\mathcal{C}$ is the solid angle subtended by the vector field $\boldsymbol{n}$ around the loop $\mathcal{C}$. This equation corresponds to the continuum limit of Eq. (30).

B. General case with spin-orbit interaction

For the lattice problem with finite SOC, Eq. (53) must be generalized to

$$\gamma_\mathcal{C} = \arg[\langle \boldsymbol{n}_j | U_{jm} | \boldsymbol{n}_m \rangle \ldots \langle \boldsymbol{n}_l | U_{lk} | \boldsymbol{n}_k \rangle \langle \boldsymbol{n}_k | U_{kj} | \boldsymbol{n}_j \rangle]. \qquad (56)$$

In the continuum limit, the unitary matrices U_{kj} become infinitesimal unitary transformations generated by an SU(2) matrix $A(t)$:

$$j \to \boldsymbol{x}(\tau),$$
$$k \to \boldsymbol{x}(t) + \dot{\boldsymbol{x}}(\tau)d\tau,$$
$$U_{kj} \to e^{iA(\tau)d\tau} = I + iA(\tau)d\tau + \mathcal{O}(d\tau^2), \qquad (57)$$

where

$$A(\tau) = \tfrac{1}{2}\sigma^a A_\mu^a \dot{x}_\mu(\tau) \qquad (58)$$

is the tangential component of the SU(2) gauge potential.

After noting that,

$$\langle \boldsymbol{n}_{\boldsymbol{x}(\tau+d\tau)} | e^{iA(\tau)d\tau} | \boldsymbol{n}_{\boldsymbol{x}(\tau)} \rangle = 1 + [i\langle \boldsymbol{n}_{\boldsymbol{x}(\tau)} | A(t) | \boldsymbol{n}_{\boldsymbol{x}(\tau)} \rangle$$
$$- \langle \boldsymbol{n}_{\boldsymbol{x}(\tau)} | \partial_\tau | \boldsymbol{n}_{\boldsymbol{x}(\tau)} \rangle]d\tau + \mathcal{O}(d\tau^2),$$

and following the same steps that appear in the derivation of Eq. (54), we obtain

$$\gamma_\mathcal{C} = i \oint_\mathcal{C} \langle \boldsymbol{n} | \mathcal{D}_\mu | \boldsymbol{n} \rangle dx_\mu \equiv \oint_\mathcal{C} \mathcal{A}_\mu dx^\mu. \qquad (59)$$

Here, we have introduced the covariant derivative

$$\mathcal{D}_\mu \equiv \partial_\mu - \frac{i\sigma^a}{2} A_\mu^a, \qquad (60)$$

and the covariant Berry connection

$$\mathcal{A}_\mu = i\langle \boldsymbol{n} | \partial_\mu | \boldsymbol{n} \rangle + \tfrac{1}{2} n^a A_\mu^a, \qquad (61)$$

to make the gauge invariance of $\gamma_\mathcal{C}$ more explicit.

We can now use Stokes theorem to convert the closed integral of Eq. (59) into an integral over the area $S_\mathcal{C}$:

$$\oint_\mathcal{C} \mathcal{A}_\mu dx^\mu = \int_{S_\mathcal{C}} [\partial_\mu \mathcal{A}_\nu - \partial_\nu \mathcal{A}_\mu] d^2\sigma^{\mu\nu}$$
$$= \frac{1}{2} \int_{S_\mathcal{C}} \left[\partial_\mu \left(n^a A_\nu^a\right) - \partial_\nu \left(n^a A_\mu^a\right)\right] d^2\sigma^{\mu\nu}$$
$$+ \frac{1}{2} \int_{S_\mathcal{C}} \boldsymbol{n} \cdot [\partial_\mu \boldsymbol{n} \times \partial_\nu \boldsymbol{n}] d^2\sigma^{\mu\nu}. \qquad (62)$$

The second term is the contribution (55) that we derived for the SU(2) invariant case. While this term is zero for collinear or coplanar magnetic orderings, the first term can still be finite, implying that collinear and magnetic textures can generate an effective magnetic field if the SOC is finite. In these cases, the effective magnetic field is $B_\eta = \epsilon_{\eta\mu\nu}\partial_\mu(n^a A_\nu^a)/2$. In other words, the effective U(1) vector potential is obtained by projecting the SU(2) vector potential into the direction of the $\boldsymbol{n}$ field.

Our next goal is to find a covariant form for the two contributions that appear in Eq. (62). The integral that appears in the first term can be reexpressed as

$$\int_{S_\mathcal{C}} \left[\partial_\mu \left(n^a A_\nu^a\right) - \partial_\nu \left(n^a A_\mu^a\right)\right] d^2\sigma^{\mu\nu}$$
$$= \int_{S_\mathcal{C}} \left[n^a \partial_\mu A_\nu^a - n^a \partial_\nu A_\mu^a + (\partial_\mu n^a) A_\nu^a - (\partial_\nu n^a) A_\mu^a\right] d^2\sigma^{\mu\nu}$$
$$= \int_{S_\mathcal{C}} \left[n^a F_{\mu\nu}^a + n^a \varepsilon^{abc} A_\mu^b A_\nu^c + A_\nu^a \partial_\mu n^a - A_\mu^a \partial_\nu n^a\right] d^2\sigma^{\mu\nu}, \qquad (63)$$

where

$$F_{\mu\nu}^a = \partial_\mu A_\nu^a - \partial_\nu A_\mu^a - \varepsilon^{abc} A_\mu^b A_\nu^c \qquad (64)$$

refers to the non-Abelian field strength.

When applied to the vector field $\boldsymbol{n}$, the covariant derivative takes the form

$$D_\mu = \partial_\mu - L^a A_\mu^a, \qquad (65)$$

where $\boldsymbol{L}$ is the vector of SO(3) generators introduced in Eq. (8). The natural covariant extension of the solid angle

density is

$$
\begin{aligned}
&\boldsymbol{n} \cdot (D_\mu \boldsymbol{n} \times D_\nu \boldsymbol{n}) \\
&= \varepsilon^{abc} n^a \big(\delta^{bn} \partial_\mu n^n - \varepsilon^{bmn} A_\mu^m n^n \big) \big(\delta^{cl} \partial_\nu n^l - \varepsilon^{ckl} A_\nu^k n^l \big) \\
&= \varepsilon^{abc} n^a \partial_\mu n^b \partial_\nu n^c - \varepsilon^{abc} \varepsilon^{bmn} n^a A_\mu^m n^n \partial_\nu n^c \\
&\quad - \varepsilon^{abc} \varepsilon^{ckl} n^a \partial_\mu n^b A_\nu^k n^l + \varepsilon^{abc} \varepsilon^{bmn} \varepsilon^{ckl} n^a A_\mu^m A_\nu^k n^n n^l \\
&= \varepsilon^{abc} n^a \partial_\mu n^b \partial_\nu n^c - \partial_\nu n^c A_\mu^c + \partial_\mu n^b A_\nu^b + \varepsilon^{ckl} A_\mu^c A_\nu^k n^l. \quad (66)
\end{aligned}
$$

By combining this equation with Eqs. (62), (63), and (64), we find a concise covariant form of the Berry phase:

$$
\gamma_{\mathcal{C}} = \frac{1}{2} \int_{S_{\mathcal{C}}} \big[n^a F_{\mu\nu}^a + \boldsymbol{n} \cdot (D_\mu \boldsymbol{n} \times D_\nu \boldsymbol{n}) \big] d^2 \sigma^{\mu\nu}. \quad (67)
$$

This final equation is one of the key contributions of this work. This equation simply tells us that the strength of the effective U(1) gauge field that is generated by the localized magnetic moments is the sum of the covariant scalar spin chirality and the the projection of the SU(2) field strength along the local direction $\boldsymbol{n}$ of the localized moments [44,45]. This is essentially the same result that was obtained in Eq. (48) by working on the lattice and taking the long-wavelength limit at the end of the process.

Another interesting aspect of this derivation is that it can be immediately generalized to the case of time-dependent magnetic configurations by allowing the Greek indices μ and ν to run from 0 to d, where 0 is the time coordinate and the d is the spatial dimension of the system under consideration. The zeroth component of the SU(2) vector potential arises from a Zeeman coupling between the spin of the conduction electrons and an external magnetic field $\boldsymbol{H}$,

$$
A_0^a = -\frac{g\mu_B}{2} H^a, \quad (68)
$$

where g is the g factor of the electron and μ_B is the Bohr magneton. The action that results from adding the Zeeman term to the effective Hamiltonian in Eq. (3),

$$
S[\Psi] = \int dt (d\boldsymbol{x} \Psi^\dagger i \partial_t \Psi - \mathcal{H}), \quad (69)
$$

preserves the invariance under time-dependent transformations of the local spin reference frame [41]

$$
\Psi \to \mathcal{U}\Psi, \quad A_\mu^a \sigma^a \to \mathcal{U} A_\mu^a \sigma^a \mathcal{U}^{-1} - 2i(\partial_\mu \mathcal{U})\mathcal{U}^{-1}, \quad (70)
$$

where Ψ is the electronic wave function in the continuum and $\mathcal{U} = e^{i\theta^a(\boldsymbol{x},t)\sigma^a/2}$. Equation (70) generalizes the time-independent rotations of the local reference frame in Eqs. (36)–(38) that were introduced for the lattice Hamiltonian. The *effective* electromagnetic field tensor produced by a time-dependent configuration of the local magnetic moments is then given by

$$
\tfrac{1}{2}\big[n^a F_{\mu\nu}^a + \boldsymbol{n} \cdot (D_\mu \boldsymbol{n} \times D_\nu \boldsymbol{n}) \big], \quad (71)
$$

where $0 \leqslant \mu, \nu \leqslant d$ and the strength of the SU(2) gauge field is still given by Eq. (64). This equation generalizes then well-known result for SU(2) invariant systems [38].
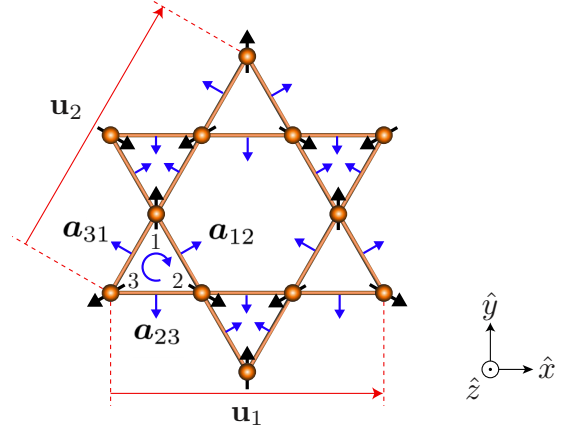

FIG. 3. Uniform 120° magnetic ordering (black arrows) on the kagome lattice. This is a straightforward extension of the single triangle state shown in Fig. 2. The clockwise circulation indicates the bond orientation. The in-plane components of the SOC vectors $\boldsymbol{a}_{12}^\perp$, $\boldsymbol{a}_{23}^\perp$, $\boldsymbol{a}_{31}^\perp$ are indicated with blue arrows. $\boldsymbol{u}_{1,2}$ are the primitive lattice vectors of the Bravais lattice.

VI. MOMENTUM-SPACE BERRY CURVATURE

In this section we will discuss a few examples to apply the notion of the generalized Berry curvature that was introduced in previous sections. In particular, we will consider an extended version of the model Hamiltonian (3) that includes potentially anisotropic exchange interactions between the local moments:

$$
\mathcal{H} = \mathcal{H}_t + \mathcal{H}_J + \mathcal{H}_H, \quad (72)
$$

where $\mathcal{H}_t$ and $\mathcal{H}_K$ have been introduced in Eq. (3) and

$$
\mathcal{H}_H = \sum_{\langle jk \rangle} S_j^\mu \mathcal{J}_{jk}^{\mu\nu} S_k^\nu. \quad (73)
$$

We will consider different 2D and 3D variants of this model comprising single or vertically stacked kagome layers. The first case corresponds to a very simple version of the model, which is useful for illustrating the connection between real-space Berry curvature introduced in the previous sections and the resulting momentum-space Berry curvature and AHE.

A. Single kagome layer

We will first assume that $\mathcal{H}_t$ is a tight-binding Hamiltonian on a single kagome layer with nearest-neighbor hopping t and that $\mathcal{H}_H$ stabilizes the ground-state magnetic ordering shown in Fig. 3: $\boldsymbol{S}_j = S\boldsymbol{n}_j$, with

$$
\boldsymbol{n}_1 = \hat{y}, \quad \boldsymbol{n}_2 = \frac{\sqrt{3}\hat{x}}{2} - \frac{\hat{y}}{2}, \quad \boldsymbol{n}_3 = \frac{-\sqrt{3}\hat{x}}{2} - \frac{\hat{y}}{2}. \quad (74)
$$

The SOC vectors introduced in Eq. (5) are

$$
\begin{aligned}
\boldsymbol{a}_{23} &= \cos\theta \, \boldsymbol{a}_{23}^\perp + \sin\theta \hat{z}, \\
\boldsymbol{a}_{31} &= \cos\theta \, \boldsymbol{a}_{31}^\perp + \sin\theta \hat{z}, \\
\boldsymbol{a}_{12} &= \cos\theta \, \boldsymbol{a}_{12}^\perp + \sin\theta \hat{z}, \quad (75)
\end{aligned}
$$

where $\boldsymbol{a}_{ij}^\perp = -\epsilon_{ijk} \boldsymbol{n}_k$. Before proceeding with the actual calculation, it is instructive to analyze the distribution of the
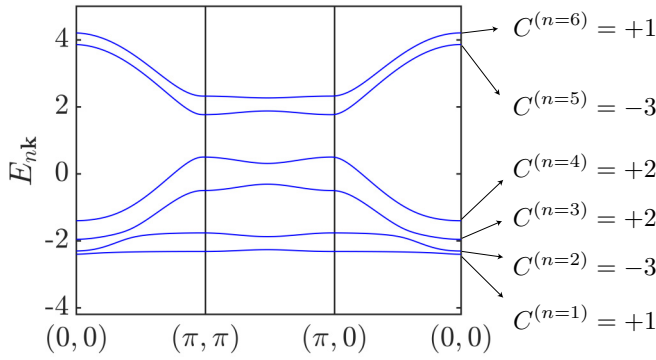
FIG. 4. Band structure of the tight-binding model of Eq. (77) for Hamiltonian parameters $J = 0.5t$, $\alpha = 0.2\pi$, $\theta = 0$.

real-space Berry curvature in the double-exchange limit $J/t \rightarrow \infty$. For $\theta = \frac{\pi}{2}$, the SOC vectors $\boldsymbol{a}_{ij}$ are collinear and parallel to the $\hat{z}$ axis. The Berry phase γ_{123} picked up by an electron that moves around the triangle 123 (see Fig. 3) is equal to π (the same is true for the hexagonal plaquettes).[2] Given that these π phases remain invariant under time-reversal symmetry, there is no effective magnetic field in real space. The tight-binding spectrum of the double-exchange Hamiltonian exhibits two Dirac points at the K points of the Brillouin zone (BZ): $(\pm\frac{4\pi}{3u}, 0)$ with $u \equiv |\boldsymbol{u}_1|$. In the opposite limit of in-plane SOC vectors ($\theta = 0$), the Berry phase becomes $\gamma_{123} = \pi - 6\alpha$ to first order in the strength of the SOC ($\alpha_{kj} \equiv \alpha$). The resulting effective magnetic flux per triangle gaps out the two Dirac points, giving rise to a finite Chern number $C = -\text{sign}(\alpha)$ of the lower band of the massive Dirac fermions.

In the more general case (away from the double-exchange limit), we need to consider six bands. The matrix of $\mathcal{H}_t + \mathcal{H}_J$ in momentum space is the 6×6 matrix

$$[H_{\boldsymbol{k}}] = \begin{bmatrix} H_{\boldsymbol{k}}^{11} & H_{\boldsymbol{k}}^{12} & (H_{\boldsymbol{k}}^{31})^{\dagger} \\ (H_{\boldsymbol{k}}^{12})^{\dagger} & H_{\boldsymbol{k}}^{22} & H_{\boldsymbol{k}}^{23} \\ H_{\boldsymbol{k}}^{31} & (H_{\boldsymbol{k}}^{23})^{\dagger} & H_{\boldsymbol{k}}^{33} \end{bmatrix} \quad (76)$$

with

$$H_{\boldsymbol{k}}^{12} = t e^{i\frac{\alpha}{2}\boldsymbol{\sigma}\cdot\boldsymbol{a}_{12}}(1 + e^{-i\boldsymbol{k}\cdot(\boldsymbol{u}_2 - \boldsymbol{u}_1)}),$$

$$H_{\boldsymbol{k}}^{23} = t e^{i\frac{\alpha}{2}\boldsymbol{\sigma}\cdot\boldsymbol{a}_{23}}(1 + e^{-i\boldsymbol{k}\cdot\boldsymbol{u}_1}), \quad H_{\boldsymbol{k}}^{31} = t e^{i\frac{\alpha}{2}\boldsymbol{\sigma}\cdot\boldsymbol{a}_{31}}(1 + e^{i\boldsymbol{k}\cdot\boldsymbol{u}_2}),$$

$$H_{\boldsymbol{k}}^{11} = -\frac{JS}{2}\boldsymbol{n}_1\cdot\boldsymbol{\sigma}, \quad H_{\boldsymbol{k}}^{22} = -\frac{JS}{2}\boldsymbol{n}_2\cdot\boldsymbol{\sigma}, \quad H_{\boldsymbol{k}}^{33} = -\frac{JS}{2}\boldsymbol{n}_3\cdot\boldsymbol{\sigma}.$$

In the absence of SOC ($\alpha = 0$), the tight-binding model hosts multiple Dirac points. As explained above, these Dirac points are gapped out for finite SOC ($\alpha \neq 0$) as long as the in-plane component of $\boldsymbol{a}_{ij}$ is nonzero. The resulting energy bands become topologically nontrivial, namely, they acquire a finite

---

[2] From the geometric approach, the Berry phase γ_{123} is equal to the solid angle of the spherical *nonagon* spanned by $\boldsymbol{n}_1, \boldsymbol{v}_{12}, \boldsymbol{w}_{12}, \boldsymbol{n}_2, \boldsymbol{v}_{23}, \boldsymbol{w}_{23}, \boldsymbol{n}_3, \boldsymbol{v}_{31}, \boldsymbol{w}_{32}$. In the present example, the nine unit vectors are coplanar, implying that the solid angle is 2π and $\gamma_{123} = \pi$. The same result can be obtained using the algebraic approach [see Eqs. (42)–(44)].

Chern number. We note that this result is consistent with our simple analysis of the double-exchange limit. As an example, for $J = 0.5t$, $\alpha = 0.2\pi$, and $\theta = 0$, the Chern numbers of each band are $C^{(n=1)} = 1$, $C^{(n=2)} = -3$, $C^{(n=3)} = 2$, $C^{(n=4)} = 2$, $C^{(n=5)} = -3$, and $C^{(n=6)} = 1$, where $n = 1$ ($n = 6$) refers to the lowest (highest) energy band. The resulting energy bands for this example are shown in Fig. 4. Note, however, that these bands are not adiabatically connected with the six bands that are obtained in the double-exchange limit (three low-energy bands separated by an energy J from the three high-energy bands) because the Chern numbers in the double-exchange limit must satisfy the property $C^{(n)} = -C^{(n+3)}$ for $1 \leqslant n \leqslant 3$. This is just a consequence of the opposite sign of the real-space Berry curvature for bands of opposite spin, i.e., aligned or antialigned with the local moments.

B. Vertically stacked kagome layers

We first consider a toy model of vertically stacked kagome layers with an SU(2) invariant hopping between adjacent layers. The intralayer magnetic ordering is assumed to be the same uniform 120° structure that we used in the previous 2D analysis, while the interlayer ordering is assumed to be ferromagnetic. For concreteness, we will assume that the interlayer hopping is finite only between nearest-neighbor (t_z^1) and next-nearest-neighbor (t_z^2) sites on adjacent kagome layers. The resulting interlayer Hamiltonian in momentum space is

$$\tilde{H}_{\boldsymbol{k}}^{\text{inter}} = \begin{bmatrix} \tilde{H}_{\boldsymbol{k}}^{11} & \tilde{H}_{\boldsymbol{k}}^{12} & (\tilde{H}_{\boldsymbol{k}}^{31})^{\dagger} \\ (\tilde{H}_{\boldsymbol{k}}^{12})^{\dagger} & \tilde{H}_{\boldsymbol{k}}^{22} & \tilde{H}_{\boldsymbol{k}}^{23} \\ \tilde{H}_{\boldsymbol{k}}^{31} & (\tilde{H}_{\boldsymbol{k}}^{23})^{\dagger} & \tilde{H}_{\boldsymbol{k}}^{33} \end{bmatrix}, \quad (77)$$

where

$$\tilde{H}_{\boldsymbol{k}}^{12} = 2t_z^2 \cos(\boldsymbol{k}\cdot\boldsymbol{u}_3)(1 + e^{-i\boldsymbol{k}\cdot(\boldsymbol{u}_2 - \boldsymbol{u}_1)}),$$

$$\tilde{H}_{\boldsymbol{k}}^{23} = 2t_z^2 \cos(\boldsymbol{k}\cdot\boldsymbol{u}_3)(1 + e^{-i\boldsymbol{k}\cdot\boldsymbol{u}_1}),$$

$$\tilde{H}_{\boldsymbol{k}}^{31} = 2t_z^2 \cos(\boldsymbol{k}\cdot\boldsymbol{u}_3)(1 + e^{i\boldsymbol{k}\cdot\boldsymbol{u}_2}),$$

$$\tilde{H}_{\boldsymbol{k}}^{11} = 2t_z^1 \cos(\boldsymbol{k}\cdot\boldsymbol{u}_3), \quad \tilde{H}_{\boldsymbol{k}}^{22} = \tilde{H}_{\boldsymbol{k}}^{11}, \quad \tilde{H}_{\boldsymbol{k}}^{33} = \tilde{H}_{\boldsymbol{k}}^{11},$$

and $\boldsymbol{u}_3$ is the primitive lattice basis vector along the c axis.

We will start by considering the trivial 2D limit of zero interlayer hopping. In this limit the spectrum does not depend on k_z, i.e., it is the same for each two-dimensional layer (k_x, k_y) in momentum space. We have seen that, in the absence of SOC, each (k_x, k_y) layer hosts several Dirac points, which become nodal lines in the 3D BZ. These nodal lines are fully gapped out by a finite SOC, implying that we can introduce a k_z-independent Chern number on any (k_x, k_y) plane, $C^{(n)}(k_z)$, for each of the six bands.

The band structure obtained in the 2D limit changes qualitatively for finite interlayer hopping because the Dirac lines are gapped everywhere, except for isolated points that turn out to be Weyl points of the 3D band structure. The finite interlayer hopping leads to a k_z dependence of the single-particle dispersion and, consequently, of the Chern number $C^{(n)}(k_z)$. The Chern number remains well defined unless the (k_x, k_y) layer crosses the Weyl points and the spectrum is thus gapless. In terms of momentum-space Berry curvature, the
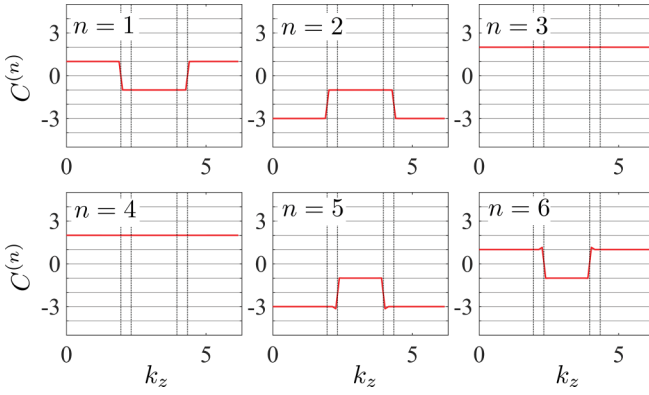
FIG. 5. Chern number $C(k_z)$ for each (k_x, k_y) plane in momentum space. The in-plane parameters are the same as in Fig. 4, while the interlayer hopping amplitudes are $t_z^1 = 0.1t$ and $t_z^2 = 0.3t$.

Weyl points are magnetic monopoles, i.e., sources and sinks of the momentum-space Berry curvature. From Gauss's law, we get that the difference between the nth band Chern numbers at the k_z and k_z' planes is equal to the sum of the charges of the Weyl points connected to that band which are enclosed by the two planes. Figure 5 shows an example of $C^{(n)}(k_z)$, where each kagome layer is identical to that in Fig. 4, and a finite interlayer hopping is included. Only the Chern numbers of the lower and the upper two bands ($n = 1, 2, 5, 6$) are changing because the $n = 2$ and 3 bands are not connected to any Weyl point.

C. Minimal model for Mn₃Sn

We will consider now a modified version of the previous model that can be regarded as a minimal Hamiltonian for the lattice and magnetic ordering of Mn_3Sn [42,46]. While this Hamiltonian is not a realistic model for Mn_3Sn, it includes the essential ingredients that are required for capturing the qualitative behavior of this material. More specifically, the model reveals the origin of the real-space Berry curvature that leads to the Weyl points that are obtained by more realistic band structure calculations [46–48] and that are the sources and drains of momentum-space Berry curvature. The crystallographic unit cell of Mn_3Sn is shown in Fig. 6(a): each unit cell includes six Mn atoms distributed in two kagome layers. As shown in Fig. 6(b), the $P6_3/mmc$ space group of this material includes the following:

(i) mirror symmetries $\mathcal{M}_i$, $i = 1, 2, 3$;

(ii) glide symmetries $\mathcal{G}_i \equiv \mathcal{M}_i' \otimes \mathcal{T}_{\frac{1}{2}}$, $i = 1, 2, 3$, with $\mathcal{T}_{\frac{1}{2}}$ the translation along c axis by $\frac{1}{2}\boldsymbol{u}_3$;

(iii) mirror symmetry $\mathcal{M}_z$ about the kagome layer;

(iv) inversion symmetry $\mathcal{I}$.

The experimental data [42] shows that Mn_3Sn displays the magnetic ordering depicted in Fig. 7, which is stable within the temperature range 50 K $< T < T_N$, with a Néel temperature $T_N \simeq 420$ K. To a good approximation, this magnetic ordering consists of a 120° structure with fixed vector spin chirality: the spin rotates anticlockwise when circulating clockwise around each triangular plaquette. Several discrete symmetries are spontaneously broken by this magnetic ordering. The residual symmetry group includes $\mathcal{M}_1$, $\mathcal{G}_2 \otimes \Theta$,
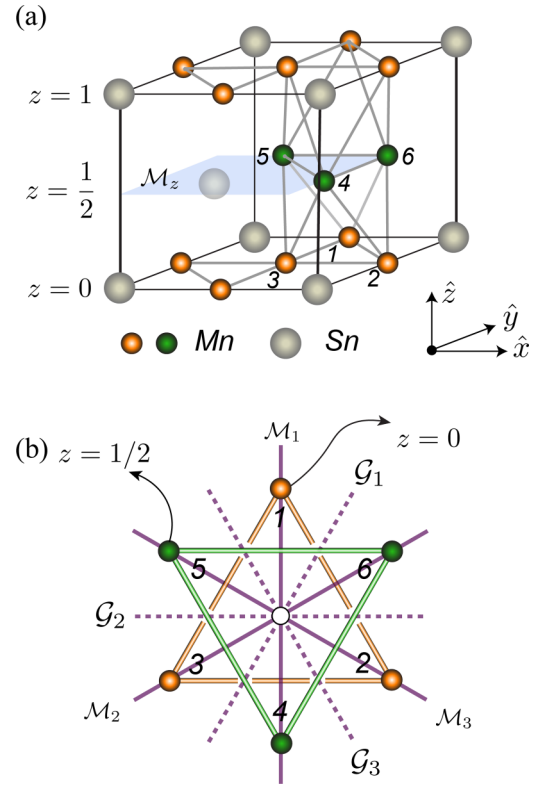

FIG. 6. (a) Crystallographic unit cell of Mn_3Sn containing six Mn atoms (3 in the $z = 0$ plane and 3 in the $\frac{1}{2}$ plane). $\mathcal{M}_z$ with $z = \frac{1}{2}$ is a mirror-symmetry plane. (b) Vertical mirror planes $\mathcal{M}_i$ and glide planes $\mathcal{G}_i$ ($i = 1, 2, 3$). The white circle at $z = \frac{1}{4}$ indicates an inversion center.

$\mathcal{M}_z \otimes \Theta$, and $\mathcal{I}$, where Θ is the time-reversal operation. The C_3 symmetry is spontaneously broken because the spin and the lattice must be rotated in *opposite directions* to keep the system invariant.

Once again, we will use the minimal Hamiltonian (3) to capture the essential features of Mn_3Sn. The site index j (or k) in Eq. (3) will be decomposed into two indices $(\alpha, \boldsymbol{r})$,
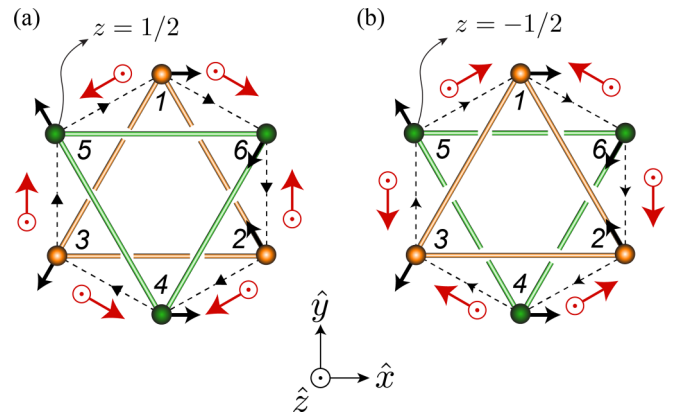

FIG. 7. Magnetic order (thick black arrows) and spin-orbital vectors $\boldsymbol{a}_{kj}$ (red arrows) on interlayer bonds connecting the orange kagome layer at $z = 0$ and the green kagome layer at (a) $z = \frac{1}{2}$ and (b) $z = -\frac{1}{2}$.

where, as shown in Fig. 6(a), $\alpha = 1, \ldots, 6$ is a sublattice index and $\boldsymbol{r}$ is the coordinate of the crystallographic unit cell. We will also assume that the above-mentioned magnetic ordering of the Mn moments is stabilized by the additional exchange interaction term that is included in Eq. (72). The corresponding orientations of the magnetic moments on each sublattice are

$$\boldsymbol{n}_1 = \boldsymbol{n}_4 = \hat{x},$$
$$\boldsymbol{n}_2 = \boldsymbol{n}_5 = -\frac{1}{2}\hat{x} + \frac{\sqrt{3}}{2}\hat{y},$$
$$\boldsymbol{n}_3 = \boldsymbol{n}_6 = -\frac{1}{2}\hat{x} - \frac{\sqrt{3}}{2}\hat{y}. \tag{78}$$

The unit vectors $\boldsymbol{a}_{jk}$ are constrained by symmetry considerations. For instance, the in-plane components of $\boldsymbol{a}_{kj}$ vanish for bonds lying in each kagome layer because of the mirror-symmetry plane $\mathcal{M}_z$, implying that $\boldsymbol{a}_{kj} = \alpha\hat{z}$. In addition, as shown in Fig. 6(a), the two kagome layers in the unit cell are related by the inversion symmetry $\mathcal{I}$: $j \to \tilde{j}$, $k \to \tilde{k}$, implying that $\boldsymbol{a}_{kj} = \boldsymbol{a}_{\tilde{k}\tilde{j}}$. By combining these results with the C_3 symmetry of the lattice, we obtain that the six in-plane hopping matrices must be the same:

$$t_{12} = t_{23} = t_{31} = t_{45} = t_{56} = t_{64} \equiv t e^{i\frac{\alpha}{2}\sigma_z}. \tag{79}$$

A similar symmetry analysis leads to the following parametrization of the interlayer hopping matrices:

$$t'_{\alpha\beta} = t' e^{i\frac{\alpha'}{2}\boldsymbol{a}'_{\alpha\beta}\cdot\boldsymbol{\sigma}}, \tag{80}$$

$$t''_{\alpha\beta} = t' e^{i\frac{\alpha'}{2}\boldsymbol{a}''_{\alpha\beta}\cdot\boldsymbol{\sigma}}, \tag{81}$$

where α, β are sublattice indices connected by interlayer bonds (see Fig. 7) and $t'_{\alpha\beta}$ ($t''_{\alpha\beta}$) are the hopping amplitudes on the interlayer bonds depicted in Fig. 7(a) [Fig. 7(b)]. The corresponding spin-orbit vectors

$$\boldsymbol{a}'_{\alpha\beta} = \pm \cos\theta' \boldsymbol{a}^\perp_{\alpha\beta} + \sin\theta'\hat{z}, \tag{82}$$

$$\boldsymbol{a}''_{\alpha\beta} = \mp \cos\theta' \boldsymbol{a}^\perp_{\alpha\beta} + \sin\theta'\hat{z} \tag{83}$$

are constrained by the mirror symmetries $\mathcal{M}_{1,2,3}$ and $\mathcal{M}_z$. The upper (lower) sign corresponds to $\alpha = 1, 2, 3$ ($\alpha = 4, 5, 6$), and the vector $\boldsymbol{a}^\perp_{\alpha\beta}$ refers to the (normalized) projection of the bond vector $\boldsymbol{a}_{\alpha\beta}$ on the basal plane

$$\boldsymbol{a}^\perp_{16} = \left(\frac{\sqrt{3}}{2}, -\frac{1}{2}, 0\right), \quad \boldsymbol{a}^\perp_{24} = \left(-\frac{\sqrt{3}}{2}, -\frac{1}{2}, 0\right),$$
$$\boldsymbol{a}^\perp_{35} = (0, 1, 0), \quad \boldsymbol{a}^\perp_{62} = \boldsymbol{a}^\perp_{35}, \quad \boldsymbol{a}^\perp_{43} = \boldsymbol{a}^\perp_{16}, \quad \boldsymbol{a}^\perp_{51} = \boldsymbol{a}^\perp_{24}. \tag{84}$$

In momentum space, the electron kinetic term is $\mathcal{H}_t = \sum_{\boldsymbol{k}} \psi^\dagger_{\boldsymbol{k}} H_{\boldsymbol{k}} \psi_{\boldsymbol{k}}$ with $\psi_{\boldsymbol{k}} = (c_{1\boldsymbol{k}}, c_{2\boldsymbol{k}}, c_{3\boldsymbol{k}}, c_{4\boldsymbol{k}}, c_{5\boldsymbol{k}}, c_{6\boldsymbol{k}})^T$ and

$$H_{\boldsymbol{k}} = \begin{bmatrix} H^{11}_{\boldsymbol{k}} & H^{21\dagger}_{\boldsymbol{k}} & H^{13}_{\boldsymbol{k}} & 0 & \tilde{H}^{15}_{\boldsymbol{k}} & \tilde{H}^{61\dagger}_{\boldsymbol{k}} \\ H^{21}_{\boldsymbol{k}} & H^{22}_{\boldsymbol{k}} & H^{32\dagger}_{\boldsymbol{k}} & \tilde{H}^{24\dagger}_{\boldsymbol{k}} & 0 & \tilde{H}^{26}_{\boldsymbol{k}} \\ H^{13\dagger}_{\boldsymbol{k}} & H^{32}_{\boldsymbol{k}} & H^{33}_{\boldsymbol{k}} & \tilde{H}^{34}_{\boldsymbol{k}} & \tilde{H}^{53\dagger}_{\boldsymbol{k}} & 0 \\ 0 & \tilde{H}^{42}_{\boldsymbol{k}} & \tilde{H}^{34\dagger}_{\boldsymbol{k}} & H^{11}_{-\boldsymbol{k}} & H^{21\dagger}_{-\boldsymbol{k}} & H^{13}_{-\boldsymbol{k}} \\ \tilde{H}^{15\dagger}_{\boldsymbol{k}} & 0 & \tilde{H}^{53}_{\boldsymbol{k}} & H^{21}_{-\boldsymbol{k}} & H^{22}_{-\boldsymbol{k}} & H^{32\dagger}_{-\boldsymbol{k}} \\ \tilde{H}^{16}_{\boldsymbol{k}} & \tilde{H}^{26\dagger}_{\boldsymbol{k}} & 0 & H^{13\dagger}_{-\boldsymbol{k}} & H^{32}_{-\boldsymbol{k}} & H^{33}_{-\boldsymbol{k}} \end{bmatrix}, \tag{85}$$

where the diagonal elements are $H^{\alpha\alpha}_{\boldsymbol{k}} = -\frac{1}{2}JS\boldsymbol{e}_\alpha \cdot \boldsymbol{\sigma}$, the off-diagonal elements $H^{\alpha\neq\beta}_{\boldsymbol{k}}$ arise from the intralayer hopping terms,

$$H^{21}_{\boldsymbol{k}} = t(1 + e^{-i\boldsymbol{k}\cdot(\boldsymbol{u}_2-\boldsymbol{u}_1)})e^{i\frac{\alpha}{2}\boldsymbol{a}\cdot\boldsymbol{\sigma}},$$
$$H^{32}_{\boldsymbol{k}} = t(1 + e^{-i\boldsymbol{k}\cdot\boldsymbol{u}_1})e^{i\frac{\alpha}{2}\boldsymbol{a}\cdot\boldsymbol{\sigma}},$$
$$H^{13}_{\boldsymbol{k}} = t(1 + e^{i\boldsymbol{k}\cdot\boldsymbol{u}_2})e^{i\frac{\alpha}{2}\boldsymbol{a}\cdot\boldsymbol{\sigma}}, \tag{86}$$

and the off-diagonal elements $\tilde{H}^{\alpha\neq\beta}_{\boldsymbol{k}}$ arise from the interlayer hopping terms

$$\tilde{H}^{61}_{\boldsymbol{k}} = t'_{16} + t''_{16}e^{i\boldsymbol{k}\cdot\boldsymbol{u}_3}, \quad \tilde{H}^{42}_{\boldsymbol{k}} = t'_{24} + t''_{24}e^{i\boldsymbol{k}\cdot\boldsymbol{u}_3},$$
$$\tilde{H}^{53}_{\boldsymbol{k}} = t'_{35} + t''_{35}e^{i\boldsymbol{k}\cdot\boldsymbol{u}_3}, \quad \tilde{H}^{34}_{\boldsymbol{k}} = t'_{43} + t''_{43}e^{-i\boldsymbol{k}\cdot\boldsymbol{u}_3},$$
$$\tilde{H}^{15}_{\boldsymbol{k}} = t'_{51} + t''_{51}e^{-i\boldsymbol{k}\cdot\boldsymbol{u}_3}, \quad \tilde{H}^{26}_{\boldsymbol{k}} = t'_{62} + t''_{62}e^{-i\boldsymbol{k}\cdot\boldsymbol{u}_3}. \tag{87}$$

D. Weyl points

For concreteness, we will consider the following set of Hamiltonian parameters: $t' = t$, $J = 2t$, $\alpha = 0.2\pi$, $\alpha' = 0.2\pi$, and $\theta' = \pi/4 \approx 0.785$. While this set does not correspond to the particular case of Mn$_3$Sn, it is enough to illustrate the physical origin of the Weyl points that appear in the band structure of this material [49]. As shown in Fig. 8(a), there are two Weyl points located at each of the K points of the BZ, connecting the fifth and the sixth bands and the seventh and the eighth bands at $k_z = 2.04$. In general, the Weyl points connecting the fifth and the sixth bands turn out to be distributed over the surface of the BZ, as shown in Figs. 8(b) and 8(c). This is not true for the other bands. Except for equivalent points related by reciprocal lattice vectors, they are classified according to the symmetries $\mathcal{M}_1$, $\mathcal{G}_2 \otimes \Theta$, $\mathcal{M}_z \otimes \Theta$, and $\mathcal{I}$.

Weyl points connecting bands n and $n + 1$ are singularities of the vector field $B^{(n)}_\rho = \sum_{\mu\nu} \epsilon_{\rho\mu\nu}\mathcal{B}^{(n)}_{\mu\nu}$, where $\mathcal{B}^{(n)}_{\mu\nu}$ is the momentum-space Berry curvature of the n band given by the Kubo formula[3]

$$\mathcal{B}^{(n)}_{\mu\nu} = -2\sum_{m\neq n} \text{Im}\left[\frac{\langle\psi_{n\boldsymbol{k}}|\partial_{k_\mu}\mathcal{H}|\psi_{m\boldsymbol{k}}\rangle\langle\psi_{m\boldsymbol{k}}|\partial_{k_\nu}\mathcal{H}|\psi_{n\boldsymbol{k}}\rangle}{(E_{n\boldsymbol{k}} - E_{m\boldsymbol{k}})^2}\right]. \tag{88}$$

$E_{n\boldsymbol{k}}$ is the dispersion relation of the nth band and $|\psi_{n\boldsymbol{k}}\rangle$ is the associated Bloch wave function. The singularity at the Weyl point is characterized by the quantized topological charge of the monopole

$$Q^{(n)} = \frac{1}{4\pi}\int_\Sigma d^2\boldsymbol{s} \cdot \boldsymbol{B}^{(n)}, \tag{89}$$

where Σ is a closed surface enclosing the Weyl point. Each Weyl point is then a source (sink) of the Berry curvature field $\boldsymbol{B}^{(n)}$ if $Q^{(n)} > 0$ ($Q^{(n)} < 0$). This charge $Q^{(n)}$ changes sign under mirror and spatial inversion transformations, while it remains invariant under time reversal. Figure 8 shows the Weyl points with $Q^{(n)} > 0$ (red color) and $Q^{(n)} < 0$ (blue color). Pairs related by the residual symmetries $\mathcal{M}_1$, $\mathcal{G}_2 \otimes \Theta$, $\mathcal{M}_z \otimes \Theta$, and $\mathcal{I}$ have opposite monopole charges.

The vector field $\boldsymbol{B}^{(n=5)}$ on the $k_z = 0$ plane is shown in Fig. 8(c). Symmetry restrictions imply that

---

[3]One could also consider the band $n + 1$ instead of n, after noticing that $\mathcal{B}^{(n+1)}_{\mu\nu} = -\mathcal{B}^{(n)}_{\mu\nu}$ near the Weyl point.
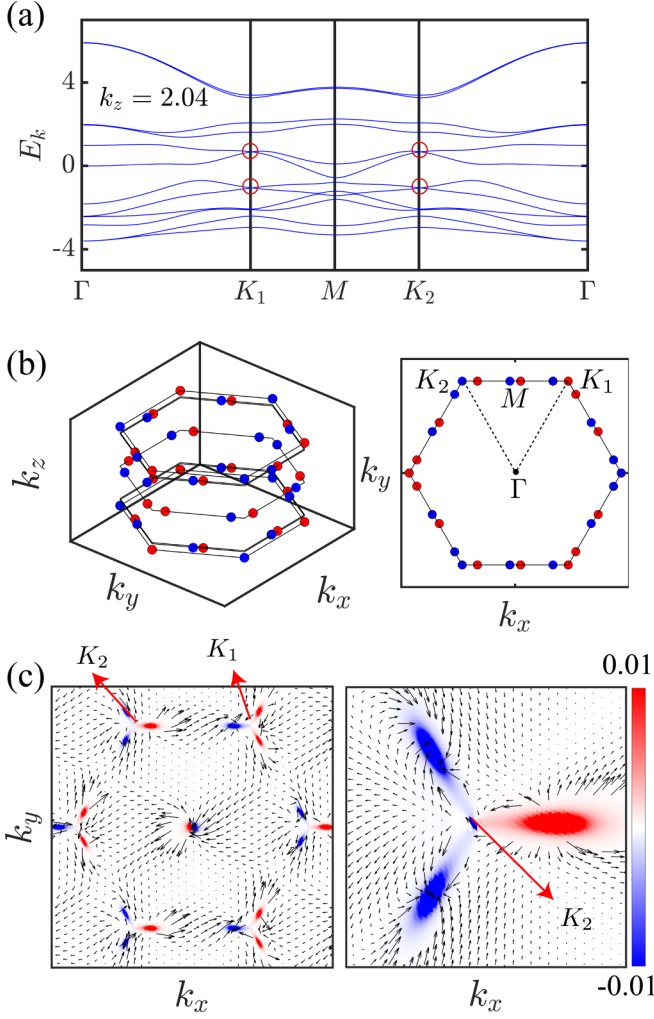
(a)

(b)

(c)

FIG. 8. (a) Band structure along symmetric paths of the BZ. Red circles indicate Weyl points. (b) Weyl points in the first BZ. Red circles correspond to $Q > 0$, while blue circles correspond to $Q < 0$. (c) Left: vector field $\boldsymbol{B}^{(5)}$ associated with the fifth band on the $q_z = 0^+$ plane (taken as $q_z = 10^{-4}$ in numerical calculation). Right: enlarged plot around the K_2 point. The model parameters are $t' = t$, $J = 2t, \alpha = 0.2\pi, \alpha' = 0.2\pi$, and $\theta' = \pi/4 \approx 0.785$.

(i) $\mathcal{M}_1 : (k_x, k_y, k_z) \rightarrow (-k_x, k_y, k_z),$

$$\left(B_x^{(n)}, B_y^{(n)}, B_z^{(n)}\right) \rightarrow \left(B_x^{(n)}, -B_y^{(n)}, -B_z^{(n)}\right); \quad (90)$$

(ii) $\mathcal{G}_2 \otimes \Theta: (k_x, k_y, k_z) \rightarrow (-k_x, k_y, -k_z),$

$$\left(B_x^{(n)}, B_y^{(n)}, B_z^{(n)}\right) \rightarrow \left(B_x^{(n)}, -B_y^{(n)}, B_z^{(n)}\right); \quad (91)$$

(iii) $\mathcal{M}_z \otimes \Theta: (k_x, k_y, k_z) \rightarrow (-k_x, -k_y, k_z),$

$$\left(B_x^{(n)}, B_y^{(n)}, B_z^{(n)}\right) \rightarrow \left(B_x^{(n)}, B_y^{(n)}, -B_z^{(n)}\right); \quad (92)$$

(iv) $\mathcal{I}: \boldsymbol{k} \rightarrow -\boldsymbol{k}, \boldsymbol{B}^{(n)} \rightarrow \boldsymbol{B}^{(n)}.$

The first two transformations imply that $B_z^{(n)} \equiv 0$ for $k_z = 0$ [k_z is fixed at 10^{-4} in Fig. 8(c) such that $B_z^{(n)} \neq 0$ near the Weyl points]. Note that $B_x^{(n)}$ remains even under the listed residual symmetry transformations, while $B_y^{(n)}, B_z^{(n)}$ are odd under some of them (e.g., the mirror-symmetry plane $\mathcal{M}_1$). This observation implies that the Hall conductivities σ_{zx} and σ_{xy} must vanish.
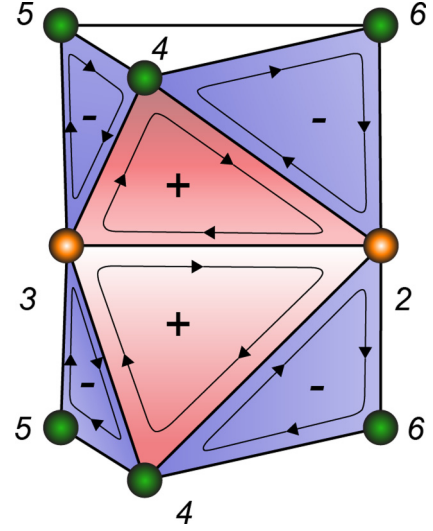

FIG. 9. Distribution of real-space Berry curvature obtained from the minimal model for Mn$_3$Sn.

At this point, it is interesting to ask what is the distribution of the *real-space* Berry curvature that leads to the distribution of *momentum-space* Berry curvature depicted in Fig. 8. This result is shown in Fig. 9. The first observation is that the effective flux is zero for intralayer triangles. The flux (Berry phase) is concentrated on the triangular plaquettes that connect different layers. The sign of the flux alternates between the two types of triangles that connect consecutive layers. Identifying the origin of the real-space Berry curvature is potentially useful for achieving a more efficient control of response functions, such as the Hall response, that are strongly influenced by the momentum-space Berry curvature. For instance, Fig. 9 indicates that changing the lattice parameter or the SOC of the *interlayer* triangles is the correct strategy for controlling momentum-space Berry curvature of Mn$_3$Sn via the modification of its real-space Berry curvature.
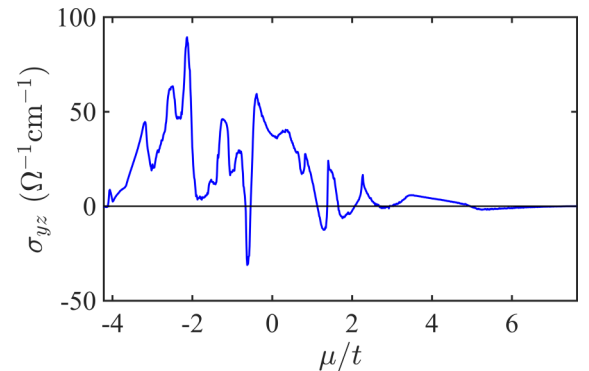

FIG. 10. Hall conductivity as a function of chemical potential μ for the same model parameters as in Fig. 8.

E. Hall conductivity

Our final step is to compute the Hall conductivity produced by the momentum-space Berry curvature. The only purpose of this calculation is to quantify the order of magnitude of the effect. We note, however, that a finite Hall conductivity is not the only measurable consequence of the momentum-space Berry curvature. Another potential consequence is a finite anomaly-related magnetoresistance that is still present in doped Weyl semimetals [50,51].

The Hall conductivity is given by

$$\sigma_{\mu\nu} = -\frac{e^2}{h} \int_{\mathrm{BZ}} \frac{d^3\boldsymbol{k}}{(2\pi)^3} \sum_n f(E_{n\boldsymbol{k}}) \mathcal{B}_{\mu\nu}^{(n)}(\boldsymbol{k}), \qquad (93)$$

where $f(x) = 1/(e^{(x-\mu)/k_BT} + 1)$ the Fermi-Dirac distribution function. The residual mirror-symmetry plane $\mathcal{M}_1$ leads to $\sigma_{zx} = \sigma_{xy} = 0$ The only nonzero component, σ_{yz}, arises from the in-plane component of the spin-orbital vector $\boldsymbol{a}_{ij}$. This is so because the mirror symmetry $\mathcal{M}_2$ times a spin rotation $R_z^{(S)}(-\frac{2\pi}{3})$ becomes an element of the residual symmetry group for $\boldsymbol{a}_{ij} \parallel \hat{z}$ on every bond.

As expected, the value of σ_{yz} depends strongly on the position of the Fermi level μ (see Fig. 10). However, it is interesting to note that the order of magnitude of the overall amplitude of the $\sigma_{yz}(\mu)$ curve coincides with the experimental value in Mn$_3$Sn [42]. In other words, our minimal model for Mn$_3$Sn not only captures the key qualitative aspects of the problem, but also the correct order of magnitude of response functions enabled by the finite momentum-space Berry curvature. This attribute of the model can be exploited for further understanding the interplay between real- and momentum-space Berry curvature induced by the combination of magnetic ordering and SOC.

Finally, we mention that the small uniform magnetization that is observed in Mn$_3$Sn should have the same origin as the spontaneous Hall conductivity. The same symmetry analysis that enables a finite σ_{yz} for the antiferromagnetic ordering depicted in Fig. 7 also enables a finite uniform orbital magnetization along the x axis that should also produce a uniform spin magnetization along the same direction via the SOC. This effect can be captured by our minimal model if we allow the antiferromagnetic state of Fig. 7 to relax into the magnetically ordered state that minimizes the total energy $\langle \mathcal{H}_t + \mathcal{H}_J + \mathcal{H}_H \rangle$.[4] As for the case of Mn$_3$Sn [42], this uniform magnetization, which must be present in any antiferromagnet that produces a spontaneous Hall effect, can be used to orient the antiferromagnetic domains and induce a net Hall conductivity.

VII. CONCLUSIONS

In summary, we have shown that the real-space Berry phase picked up by electrons when they move in a closed loop while interacting with local magnetic moments is a geometric property that combines rotation matrices associated

with the finite SOC and the underlying magnetic ordering. From a more physical point of view, the finite SOC rotates the electronic spin while the electron hops from one atomic orbital to another. This rotation enables a nontrivial Berry phase (different from 0 or π) induced by collinear and coplanar magnetic configurations. In view of the fact that collinear and coplanar magnetic orderings are more common than noncoplanar orderings, we can conclude that SOC should play a crucial role in the discovery of new materials with large topological Hall effect, or even finite-temperature Chern insulators, induced by spontaneous antiferromagnetic ordering. While material candidates can be identified by applying a simple symmetry analysis [32,52], understanding the underlying microscopic mechanism for the generation of Berry curvature is of crucial importance for the optimization and control of the effect. Understanding the microscopic mechanism is also necessary to estimate the value of the topological contribution to different response functions of interest and to anticipate the change of these response functions under the application of external fields, such as pressure, strain, or magnetic field.

Here, we have reduced this microscopic mechanism to its simplest form by considering the minimal model introduced in Eq. (3). Like for the SU(2) invariant case of zero SOC, the mechanism becomes transparent in the double-exchange limit of this model where the low-energy theory maps into a theory of spinless fermions coupled to an effective U(1) gauge field. Our work provides the first derivation of the effective U(1) gauge field produced by a given magnetic ordering in the presence of SOC. The main result is that the strength of this emergent U(1) gauge field has two covariant contributions. The first contribution is the covariant SU(2) extension of the skyrmion density in the underlying configuration of localized magnetic moments. The second contribution is simply the projection of the strength of the SU(2) gauge field produced by the SOC along the direction of the localized magnetic moments.

This simple result reveals the role of SOC in the generation of the real-space Berry curvature and, therefore, the topological Hall effect, which has been a long-standing debate for many years; see, for instance, Ref. [39] of our paper. The effect of SOC becomes particularly clear when the SOC itself can be gauged away by a local rotation of the spin reference frame. The real-space Berry curvature is then equal to the skyrmion density of the localized magnetic moments in that particular reference frame. Clearly, magnetic configurations that are collinear or coplanar in the laboratory reference frame can become noncoplanar in the new reference frame.

We have illustrated these concepts by applying them to a simple minimal model that captures the essential aspects of Mn$_3$Sn [42]. A similar analysis can in principle be applied to other materials that exhibit topological Hall effect induced by coplanar or collinear magnetic orderings [52]. Moreover, given that the SU(2) gauge field produced by the SOC is a bond variable (i.e., it depends on the relative position of the two ions connected by that bond), it is natural to expect that pressure and strain could play an important role in the external control of the topological Hall effect. This is a new control variable enabled by the SOC, in addition to the external magnetic field that controls the orientation of the localized magnetic moments via the Zeeman term. It is then clear that

---

[4]Note that in our previous analysis we assumed for simplicity that the Heisenberg term is dominant and the optimal magnetic ordering is then determined by minimization of this term.

SOC is crucially important for expanding the spectrum of materials and external fields that can be used to produce and control potentially large topological contributions to response functions.

Finally, we remark that this work is complementary to the quantitatively more accurate first-principle calculations in that it aims to understand *how* SOC can generate a topological Hall effect. Although it is already known from first-principle calculations that collinear and noncollinear magnetic orderings can produce anomalous Hall effect in the presence of SOC, the underlying microscopic mechanism remains unclear in those treatments. Minimal effective models, such as the *s-d* model considered here, reveal these mechanisms and provide a crucial insight for enhancing and controlling this phenomenon in different materials. In addition, we note that the *s-d* model can also be obtained from an unconstrained mean-field treatment of *itinerant magnets*, where the classical spin variables correspond to expectation values of the *itinerant* magnetic moment on each atom [24].

[1] E. Dagotto, T. Hotta, and A. Moreo, Phys. Rep. **344**, 1 (2001).

[2] Y. Tokura and N. Nagaosa, Science **288**, 462 (2000).

[3] A. P. Ramirez, J. Phys.: Condens. Matter **9**, 8171 (1997).

[4] L. M. Rodriguez-Martinez and J. P. Attfield, Phys. Rev. B **54**, R15622 (1996).

[5] N. Nagaosa, J. Phys. Soc. Jpn. **75**, 042001 (2006).

[6] E. H. Hall, The London, Edinburgh, and Dublin Philosophical Magazine and Journal of Science **12**, 157 (1881).

[7] A. W. Smith, Phys. Rev. **17**, 23 (1921).

[8] C. M. Hurd, *The Hall Effect in Metals and Alloys* (Plenum, New York, 1972).

[9] Y. Taguchi, Y. Oohara, H. Yoshizawa, N. Nagaosa, and Y. Tokura, Science **291**, 2573 (2001).

[10] R. Karplus and J. M. Luttinger, Phys. Rev. **95**, 1154 (1954).

[11] J. Smit, Physica (Amsterdam) **24**, 39 (1958).

[12] L. Berger, Phys. Rev. B **2**, 4559 (1970).

[13] W.-L. Lee, S. Watauchi, V. L. Miller, R. J. Cava, and N. P. Ong, Science **303**, 1647 (2004).

[14] T. Miyasato, N. Abe, T. Fujii, A. Asamitsu, S. Onoda, Y. Onose, N. Nagaosa, and Y. Tokura, Phys. Rev. Lett. **99**, 086602 (2007).

[15] S. Onoda, N. Sugimoto, and N. Nagaosa, Phys. Rev. B **77**, 165103 (2008).

[16] D. J. Thouless, M. Kohmoto, M. P. Nightingale, and M. den Nijs, Phys. Rev. Lett. **49**, 405 (1982).

[17] M. V. Berry, Proc. R. Soc. London A **392**, 45 (1984).

[18] M. Onoda and N. Nagaosa, J. Phys. Soc. Jpn. **71**, 19 (2002).

[19] T. Jungwirth, Q. Niu, and A. H. MacDonald, Phys. Rev. Lett. **88**, 207208 (2002).

[20] J. Ye, Y. B. Kim, A. J. Millis, B. I. Shraiman, P. Majumdar, and Z. Tešanović, Phys. Rev. Lett. **83**, 3737 (1999).

[21] Y. Aharonov and D. Bohm, Phys. Rev. **115**, 485 (1959).

[22] P. Matl, N. P. Ong, Y. F. Yan, Y. Q. Li, D. Studebaker, T. Baum, and G. Doubinina, Phys. Rev. B **57**, 10248 (1998).

[23] S. H. Chun, M. B. Salamon, Y. Lyanda-Geller, P. M. Goldbart, and P. D. Han, Phys. Rev. Lett. **84**, 757 (2000).

[24] K. Ohgushi, S. Murakami, and N. Nagaosa, Phys. Rev. B **62**, R6065 (2000).

[25] R. Shindou and N. Nagaosa, Phys. Rev. Lett. **87**, 116801 (2001).

[26] I. Martin and C. D. Batista, Phys. Rev. Lett. **101**, 156402 (2008).

[27] Y. Kato, I. Martin, and C. D. Batista, Phys. Rev. Lett. **105**, 266405 (2010).

[28] Y. Akagi and Y. Motome, J. Phys. Soc. Jpn. **79**, 083711 (2010).

[29] K. Barros, J. W. F. Venderbos, G.-W. Chern, and C. D. Batista, Phys. Rev. B **90**, 245119 (2014).

[30] C. D. Batista, S.-Z. Lin, S. Hayami, and Y. Kamiya, Rep. Prog. Phys. **79**, 084504 (2016).

[31] R. Ozawa, S. Hayami, and Y. Motome, Phys. Rev. Lett. **118**, 147205 (2017).

[32] H. Chen, Q. Niu, and A. H. MacDonald, Phys. Rev. Lett. **112**, 017205 (2014).

[33] X. G. Wen, F. Wilczek, and A. Zee, Phys. Rev. B **39**, 11413 (1989).

[34] N. Nagaosa and P. A. Lee, Phys. Rev. Lett. **64**, 2450 (1990).

[35] P. A. Lee and N. Nagaosa, Phys. Rev. B **46**, 5621 (1992).

[36] C. Zener, Phys. Rev. **81**, 440 (1951).

[37] P. W. Anderson and H. Hasegawa, Phys. Rev. **100**, 675 (1955).

[38] G. E. Volovik, *The Universe in a Helium Droplet* (Oxford University Press, New York, 2003).

[39] T. Tomizawa and H. Kontani, Phys. Rev. B **80**, 100401(R) (2009).

[40] J. Fröhlich and U. M. Studer, Rev. Mod. Phys. **65**, 733 (1993).

[41] I. V. Tokatly, Phys. Rev. Lett. **101**, 106601 (2008).

[42] S. Nakatsuji, N. Kiyohara, and T. Higo, Nature (London) **527**, 212 (2015).

[43] N. J. Ghimire, A. S. Botana, J. S. Jiang, J. Zhang, Y. S. Chen, and J. F. Mitchell, Nat. Commun. **9**, 3280 (2018).

[44] F. V. Gubarev and V. I. Zakharov, Int. J. Mod. Phys. A **17**, 157 (2002).

[45] F. V. Gubarev, Phys. Rev. D **69**, 114502 (2004).

[46] N. Ito and K. Nomura, J. Phys. Soc. Jpn. **86**, 063703 (2017).

[47] J. Kübler and C. Felser, Europhys. Lett. **108**, 67001 (2014).

[48] J. Kübler and C. Felser, Europhys. Lett. **120**, 47002 (2018).

[49] H. Yang, Y. Sun, Y. Zhang, W.-J. Shi, S. S. P. Parkin, and B. Yan, New J. Phys. **19**, 015008 (2017).

[50] H. Ishizuka and N. Nagaosa, Phys. Rev. B **99**, 115205 (2019).

[51] H. Ishizuka and N. Nagaosa, arXiv:1807.08147.

[52] L. Šmejkal, R. González-Hernández, T. Jungwirth, and J. Sinova, arXiv:1901.00445.